

THE DISSECTION OF ABELL 2744: A RICH CLUSTER GROWING THROUGH MAJOR AND MINOR MERGERS.

MATT S. OWERS¹, SCOTT W. RANDALL², PAUL E.J. NULSEN², WARRICK J. COUCH¹, LAURENCE P. DAVID², JOSHUA C. KEMPNER

Draft version October 28, 2018

ABSTRACT

New *Chandra* X-ray data and extensive optical spectroscopy, obtained with AAOmega on the 3.9 m Anglo-Australian Telescope, are used to study the complex merger taking place in the galaxy cluster Abell 2744. Combining our spectra with data from the literature provides a catalog of 1237 redshifts for extragalactic objects lying within 15' of the cluster center. From these, we confirm 343 cluster members projected within 3 Mpc of the cluster center. Combining positions and velocities, we identify two major substructures, corresponding to the remnants of two major subclusters. The new data are consistent with a post core passage, major merger taking place along an axis that is tilted well out of the plane of the sky, together with an interloping minor merger. Supporting this interpretation, the new X-ray data reveal enriched, low entropy gas from the core of the approaching, major subcluster, lying $\sim 2'$ north of the cluster center, and a shock front to the southeast of the previously known bright, compact core associated with the receding subcluster. The X-ray morphology of the compact core is consistent with a Bullet-like cluster viewed from within $\sim 45^\circ$ of the merger axis. An X-ray peak $\sim 3'$ northwest of the cluster center, with an associated cold front to the northeast and a trail of low entropy gas to the south, is interpreted as the remnant of an interloping minor merger taking place roughly in the plane of the sky. We infer approximate paths for the three merging components.

Subject headings: galaxies: clusters: individual (Abell 2744) — X-rays: galaxies: clusters

1. INTRODUCTION

In a universe where structure grows hierarchically, clusters of galaxies are the latest structures to collapse and virialize (e.g., Springel et al. 2006). There are three main modes of mass accretion onto rich clusters of galaxies: the steady infall of matter from the surrounding filamentary large scale structures, the discrete accretion of group-sized objects, and the extreme event of a major cluster-cluster merger. The latter are the most energetic events known in the Universe (Markevitch et al. 1998) and result in the violent reassembly of the cluster. Such a dramatic reconfiguration of the cluster results in a rapid change in the environment of its member galaxies, although what effect this has the galaxies themselves is yet to be fully understood. This is in part due to the complex nature of cluster mergers and, hence, the difficulty in obtaining a detailed picture of their properties.

The well known Butcher-Oemler effect (hereafter BO-effect; Butcher & Oemler 1978, 1984), that the fraction of blue galaxies in the cores of rich clusters is significantly lower at the present epoch than it was ~ 2.5 Gyrs or more ago, reveals that a significant fraction of cluster galaxies have undergone rapid transformation in star-forming properties over the intervening period. Furthermore, the observed increase with redshift in the fraction of spiral galaxies in clusters at the expense of a commensurate decline in the S0 fraction (Dressler et al. 1997; Fasano et al. 2000; Desai et al. 2007; Just et al. 2010) reveals a corresponding rapid evolution in galaxy morphology.

While the BO effect appears to be widespread, the scatter in the blue galaxy fraction is large at all redshifts ($z > 0.2$) and exceeds the uncertainties in the measurements (Butcher & Oemler 1984). This indicates some internal cluster-specific mechanism is responsible for the scatter and Margoniner et al. (2001) found that a large portion of this scatter can be attributed to the richness of a cluster, where less rich clusters have a higher blue fraction. Another intriguing possibility is that the scatter is driven by the hierarchical formation of clusters, in particular cluster mergers, which become more common with increasing redshift. Here it is quite conceivable that they would lead to an increased blue galaxy fraction through triggering star formation in the member galaxies (Kauffmann 1995; Metevier et al. 2000; Miller et al. 2006).

In this context, spectroscopic observations of the Coma cluster have revealed a tantalizing correlation between the spatial distribution of post-starburst galaxies and regions involved in merger activity (Caldwell et al. 1993; Caldwell & Rose 1997; Poggianti et al. 2004). These observations strongly suggest that the merging process can affect the star-forming properties of the cluster galaxies. This spurred Caldwell & Rose (1997) to conduct a further study to search for “abnormal” spectrum galaxies, similar to those BO galaxies found at higher redshift, in four additional nearby clusters, three of which were selected on the basis of harboring clear substructure. Although their study was limited to galaxies of early-type morphology, the results indicated that there is a significant fraction of abnormal-type galaxies in nearby rich clusters and, most intriguingly, the triggering of starbursts leading to abnormal spectra occurs during the core passage phase of a merger. Recently, Hwang & Lee (2009) have

¹Center for Astrophysics and Supercomputing, Swinburne University of Technology, Hawthorn, VIC 3122, Australia; mowers@astro.swin.edu.au

²Harvard Smithsonian Center for Astrophysics, 60 Garden Street, Cambridge, MA 02138, USA

provided further evidence for this scenario by comparing the galaxy properties in the post-core passage merger Abell 168 and the pre-core passage merger Abell 1750. Furthermore, radio observations have revealed that clusters which harbor evidence for major merger activity show an increase in radio activity amongst their galaxies (Miller & Owen 2003; Miller et al. 2006; Venturi et al. 2001, 2000; Johnston-Hollitt et al. 2008). However, there are counter-examples (Venturi et al. 2002), suggesting that the merger phase is an important factor. According to the simulations of Bekki et al. (2010), this evolution may be driven by the significant increase in ICM pressure that a galaxy is exposed to during a cluster merger, in particular when the galaxy passes through regions affected by shocks during the core passage stage of the merger (see also Roettiger et al. 1996). *Therefore, an understanding of the merger dynamics and merging history of a cluster is critical when attempting to disentangle the effects leading to the triggering and halting of star formation in cluster galaxies.*

The rich X-ray luminous cluster Abell 2744 at $z = 0.3$ (also known as AC118; Couch & Newell 1984) is an interesting test case, being both a well known merging cluster and one that exhibits a significant BO effect. Two previous studies have addressed the dynamical state of the merger occurring in the core of Abell 2744. The first was the *Chandra*-based study of Kempner & David (2004, hereafter KD04), who showed that Abell 2744 is undergoing a major merger in approximately the north-south direction. The second was conducted by Boschin et al. (2006) who used 85 cluster member spectra to show that the merger has a significant velocity component along the line of sight, as suggested by KD04 (see also; Girardi & Mezzetti 2001), and estimated the mass ratio of the merging subclusters to be $\sim 3 : 1$. This merger also quite naturally explains why Abell 2744 hosts one of the most luminous known radio haloes covering its central 1.8 Mpc, as well as a large radio relic at a distance of about 2 Mpc from the cluster center (Giovannini et al. 1999; Govoni et al. 2001a,b). The presence of a significant blue galaxy excess—a blue fraction that was 2.2 ± 0.3 times that seen in the same core regions of nearby clusters—was first measured photometrically and confirmed spectroscopically by Couch & Sharples (1987), who found the cluster to have a blue galaxy fraction of $\sim 25\%$. Moreover, the spectroscopic study showed that the blue galaxy population in Abell 2744 was dominated by starburst and post-starburst galaxies. Abell 2744 therefore provides an excellent laboratory for studying the link between major merger activity and star formation activity in cluster galaxies. This paper reports the first step of this study, which is to determine more precisely the *phase* and *history* of Abell 2744’s merger, in particular whether it is in a pre-core or post-core passage phase.

As has been shown previously (e.g., Zabludoff & Zaritsky 1995; Barrena et al. 2007; Maurogordato et al. 2008; Owers et al. 2009c; Ma et al. 2009, 2010), the combination of high quality X-ray imaging and spectroscopy with comprehensive optical spectroscopy provides a powerful toolkit for disentangling the complex dynamics of cluster mergers. In this paper, we combine new *Chandra* observations, which provide an additional 100ks of data to the existing 25ks analyzed in KD04, with

new AAT/AAOmega optical multi-object spectroscopy (MOS), which roughly doubles the number of spectroscopically confirmed cluster members over a 3 Mpc radius region, and also doubles the number of cluster member spectra within the central regions studied by Boschin et al. (2006). These data sets are used both to detect substructure in Abell 2744, which is related to the merger activity, and to provide a more up-to-date interpretation of the merging history.

The outline of this paper is as follows. In Section 2 we present the reduction and analysis of the new *Chandra* data. In Section 3 present details of the MOS observations and data reduction, the redshift catalog, and the cluster membership allocation procedure. In Section 4 we present the methods used for substructure detection. In Section 5 we present our interpretations of the nature of the structures detected in the optical and X-ray data. In Section 6 we present our merger scenario based on the observations and interpretations presented in the paper. Finally, in Section 7 we summarize our results.

Throughout the paper, we assume a standard Λ CDM cosmology where $H_0 = 70 \text{ km s}^{-1}$, $\Omega_m = 0.3$ and $\Omega_\Lambda = 0.7$. For the assumed cosmology and at the cluster redshift ($z=0.3064$), $1''=4.52 \text{ kpc}$.

2. CHANDRA DATA

2.1. Observations and Data Reduction

Abell 2744 has been observed with *Chandra* using both the ACIS-I and ACIS-S chip arrays and we summarize the dates, exposure times and *Chandra* ObsID’s in Table 1. The data were reprocessed starting with the level 1 event files and using *CIAO* version 3.4 with the latest gain and calibration files applied (CalDB version 3.5.5). All observations were performed in Very Faint (VF) data mode, allowing 5×5 pixel islands to be used in identifying cosmic ray events, significantly helping to reduce the particle background. Observation specific bad pixel files were produced and applied and events flagged with *ASCA* grades 1, 5 and 7 were excluded. The data were filtered for periods of anomalously high background associated with flares. Standard procedures are followed in doing this, i.e., for the ACIS-I observations, point sources and the region containing the diffuse cluster emission were excluded, and a light curve was extracted in the 0.3 – 10 keV range binned in 259s intervals. The *Sherpa* `lc_clean.sl` routine was then used to identify for removal time intervals when the count rate deviated by more than 20% from the mean. No significant flares were detected, and the cleaned exposure times are listed in Table 1.

For background subtraction during spectral and imaging analyses, we use the blank sky observations³ appropriate for the chip and epoch of the observation of interest. The background files were processed in the same manner as the observations, using the same background filtering, bad pixel and gain files, and were reprojected to match the observations. The backgrounds were normalized so that the source and background counts in the 10 – 12 keV range matched. We checked for excess soft Galactic X-ray emission in the observations by extracting spectra from source-free regions and comparing to spectra extracted from the background files, finding no significant difference.

³ See <http://cxc.harvard.edu/contrib/maxim/acisbg>

Table 1
Summary of the *Chandra* observations.

Array	ObsId	Date	Exposure Time (ks)	Cleaned Exposure Time (ks)
ACIS-S	2212	2001 September 3	25.14	23.79
ACIS-I	7712	2007 September 10	8.17	8.07
ACIS-I	7915	2006 November 8	18.86	18.62
ACIS-I	8477	2007 June 10	46.5	45.91
ACIS-I	8557	2007 June 14	28.17	27.75

2.2. Image Analysis

The left panel of Figure 1 shows a background-subtracted, 0.5 – 7 keV, exposure-corrected image of Abell 2744 which has been binned using the WVT binning algorithm of Diehl & Statler (2006), which is a generalization of Cappellari & Copin (2003)’s Voronoi binning algorithm. The bin size is determined by the constraint that the signal-to-noise ratio must be ~ 5 . Prior to binning, point sources detected with *wavdetect* were removed and the regions were filled via interpolation from a surrounding background region using *dmfilth*. The exposure map was generated using standard *CIAO* procedures⁴ and accounts for the effects of vignetting, quantum efficiency (QE), QE nonuniformity, bad pixels, dithering, and effective area. The energy dependence of the effective area is accounted for by computing a weighted instrument map where the weights are computed from an absorbed MEKAL spectral model with Galactic absorption, temperature, redshift and abundance set to the average cluster values obtained in Section 2.3.1. The right panel of Figure 1 shows the background subtracted, exposure corrected image of Abell 2744 with point sources included, and with a light Gaussian smooth (FWHM=4'') applied. Abell 2744 is clearly a disturbed system, with a structure ~ 750 kpc to the northwest of the X-ray surface brightness peak (labelled northwestern interloper). Within the main X-ray structure, there are a further three substructures: one ~ 190 kpc south (labelled southern compact core), one ~ 480 kpc to the north (labelled northern core) and another ~ 220 kpc to the north of the X-ray surface brightness peak. The northern core furthest from the X-ray peak has a tail, which includes the second structure north of the X-ray peak, extending southward and curving westward towards the peak in the X-ray emission. The southern compact core has a blunted cone morphology with a prominent head and a fan-like tail of emission extending back towards the peak in the X-ray emission. There is also an edge in the surface brightness ~ 250 kpc to the southeast of the southern substructure.

The northwestern interloper appears asymmetric, with an edge just east of north and an extended tail toward the south. There also appears to be a bridge of emission connecting it to the main cluster emission. Based on a shorter *Chandra* observation, KD04 tentatively identified a cold front and bow shock on the eastern side of the northwestern interloper and also a fan-like feature extending towards the west. They concluded the northwestern interloper was moving from west to east on its way towards the cluster core. However, the deeper observations presented in Figure 1 do not confirm the exist-

tence of a bow shock and indicate the cold front on the eastern side is part of a larger northern edge, meaning the interpretation of KD04 may not be the correct one.

To emphasize the structures revealed in Figure 1 we present the residual significance map, which highlights low surface brightness structures, and the unsharp masked image, which is useful for revealing sharp structures such as shocks and cold fronts, in Figure 2. To produce the significance map, we first fit the *Chandra* image with an azimuthally symmetric β -model with best fitting values of $r_c = 471 \pm 8$ kpc, $\beta = 0.96 \pm 0.13$, R.A.=00^h14^m18.4^s and decl.=−30°23′14″.0. During the fitting of the β -model, the northwest substructure was excluded, along with point sources. This β -model accounts for the main cluster emission and is subtracted from *Chandra* image to produce a residual image which is then smoothed with a Gaussian kernel with $\sigma = 3''$. The resulting smoothed residual map is then divided by an error map to produce the residual significance map (see Neumann & Böhringer 1997; Owers et al. 2009c, for more details). The left panel in Figure 2 shows that the northwest interloper and its extended tail to the south are detected with high significance, while the northern core and southern compact core, along with the tail near the northern core, are also detected. The unsharp masked image is produced by dividing a background subtracted, exposure corrected image that was smoothed with a 4.4'' Gaussian by the same image smoothed by 22'', corresponding to physical scales of 20 kpc and 100 kpc at the cluster redshift. The unsharp masked image is shown in the right panel of Figure 2, where it can be seen that the structure in the central cluster region is very similar to that seen in the residual significance map. However, the unsharp masked image accentuates the edge to the north of the northwestern interloper and also a finger of emission extending from the northwestern interloper towards the south.

2.3. Thermodynamic maps

2.3.1. Temperature maps

To better determine the nature of the features seen in Figures 1 and 2 and to identify other regions affected by the merger activity, we produce two maps of the projected temperature distribution for Abell 2744 using complementary techniques. The first temperature map is produced using a similar method to that developed by O’Sullivan et al. (2005) and Maughan et al. (2006), which is outlined in full in Randall et al. (2008). Briefly, the X-ray image is binned to a $1''.968 \times 1''.968$ pixel size and at the position of each pixel, source and background spectra are extracted in a circular region surrounding the pixel. The radius of this region is defined adaptively so that the extracted region contains 1500 background sub-

⁴ see http://cxc.harvard.edu/ciao3.4/threads/expmap_acis_multi/

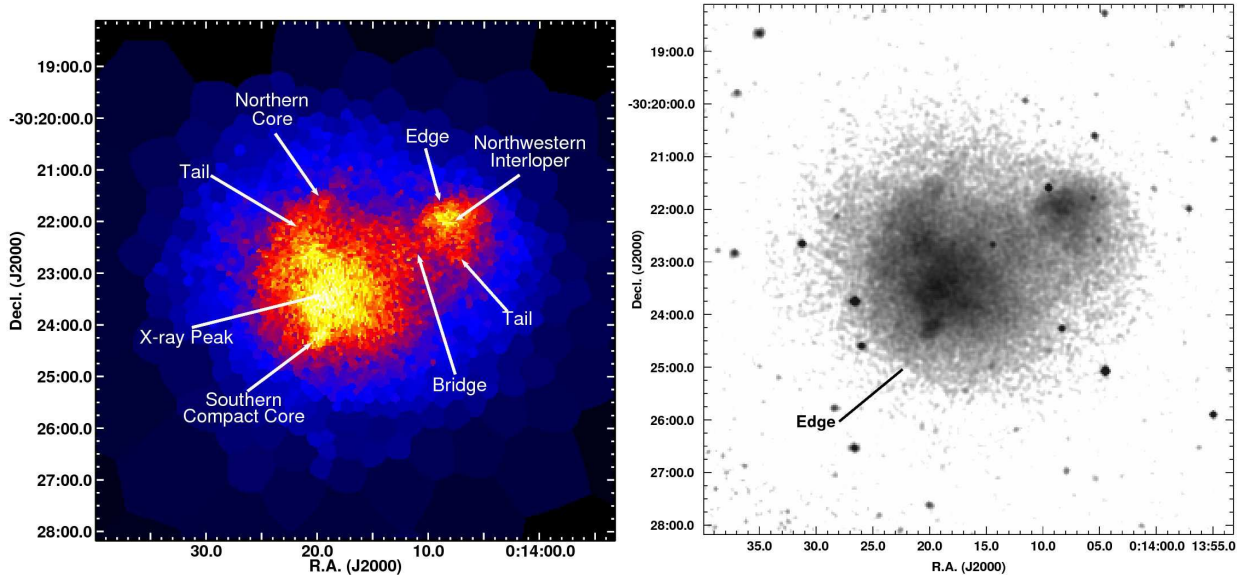


Figure 1. Background-subtracted, exposure-corrected *Chandra* images. The image in the *left panel* is binned to $S/N=5$ using the WVT algorithm and the point sources have been removed and filled using *dmfilth*. The image in the *right panel* shows the image with point sources, binned to $1''.968$ pixels and smoothed with a Gaussian kernel with $FWHM=4''$.

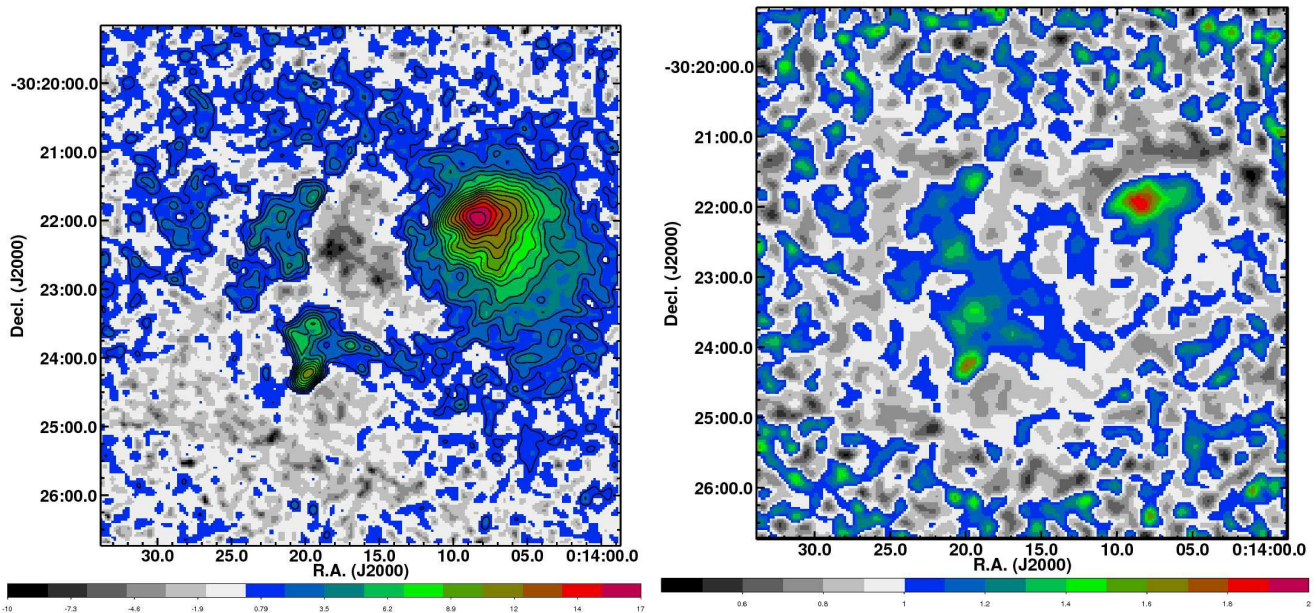


Figure 2. *Left panel:* Residual significance image produced using a similar method as in Owers et al. (2009c), i.e., an azimuthally symmetric β -model is fitted to the data (excluding the northwestern interloper and point sources) and then subtracted to produce a residual image. The residual image is then smoothed and divided by an error map to produce the residual significance map. Contours are spaced linearly in steps of 1σ in the range $1 - 17\sigma$. *Right panel:* Unsharp masked image created by dividing an exposure and background corrected image smoothed using a Gaussian kernel with $\sigma = 4.4''$ (20 kpc) by one smoothed by $\sigma = 22''$ (100 kpc).

tracted counts. The process is expedited by extracting the response files from a coarser grid. For each spectrum, an absorbed MEKAL model is fitted in the energy range $0.6 - 9.5$ keV, with the absorption column density set at the Galactic value, $N_H = 1.61 \times 10^{20} \text{ cm}^{-2}$ (Dickey & Lockman 1990), the abundance set to the global value of $Z_{ave} = 0.262$ (see below) and the temperature free to vary. This temperature map is presented in the top left panel of Figure 3. We note that this method produces a temperature map with correlated

pixels and the scale over which the pixels are correlated is not clear from the temperature map alone. Therefore, as a check we produced a second temperature map using the WVT algorithm to bin the image such that each (uncorrelated) spatial bin contains ~ 1500 background subtracted $0.5 - 7$ keV counts. We select a number of regions of interest from the temperature map shown in the top left panel of Figure 3 (marked with crosses) and we require the WVT binning algorithm to place a bin centered on each of these regions. For each bin we

extract observation-specific source spectra, corresponding count-weighted responses, and background spectra from the blank sky observations. The background spectra had their exposure times normalized so that the 9.5–12 KeV count rates match the observed rates. The spectra were re-binned so that there was at least 1 count per energy bin. The re-binned observation-specific spectra were fitted simultaneously over the 0.5–7 keV energy range within the XSPEC package (Arnaud 1996) using an absorbed MEKAL model (Kaastra 1992; Liedahl et al. 1995) with abundance, column density and redshift fixed to those values used for the non-tessellated map. The Cash statistic was minimized during fitting. This tessellated temperature map is shown in the middle left panel of Figure 3. The tessellated and non-tessellated temperature maps are in excellent agreement.

We have produced significance maps for both the tessellated and non-tessellated temperature maps which show how significant the spatial variations in temperature are when compared to the global average temperature, kT_{ave} . The significance, $\Delta(kT)$, is defined at each pixel as

$$\Delta(kT) = \begin{cases} \frac{(kT_{pix} - kT_{ave})}{\sqrt{\sigma(kT_{pix,hi})^2 + \sigma(kT_{ave,lo})^2}}, & kT_{pix} < kT_{ave}, \\ \frac{(kT_{pix} - kT_{ave})}{\sqrt{\sigma(kT_{pix,lo})^2 + \sigma(kT_{ave,hi})^2}}, & kT_{pix} \geq kT_{ave}, \end{cases} \quad (1)$$

where kT_{pix} is the temperature map value for the pixel of interest, $\sigma(kT_{pix,hi})$ and $\sigma(kT_{pix,lo})$ are the upper and lower 68% confidence limits for kT_{pix} , respectively, and $\sigma(kT_{ave,hi})$ and $\sigma(kT_{ave,lo})$ are the upper and lower 68% confidence limits for kT_{ave} , respectively. The significance maps are shown in the top right and middle right panels of Figure 3 for the non-tessellated and tessellated maps, respectively. The global average temperature, kT_{ave} , was determined from fitting spectra extracted from a ~ 900 kpc radius region containing the majority of the cluster emission with an absorbed MEKAL model, as outlined above for the tessellated maps, with the exception that the abundance was free to be fitted. We find $kT_{ave} = 9.07 \pm 0.15$ keV, while the global average abundance $Z_{ave} = 0.262 \pm 0.025$. These values are consistent with the values presented in Zhang et al. (2004).

The temperature maps reveal a rich diversity of patchy temperature structures, the most significant of which include: (i) A prominent cool ~ 5 keV region associated with the northwest interloper where the coolest gas is coincident with the compressed X-ray isophotes, indicating there is a cold front there. We also note a hint of a cool swirl heading to the south of the northwestern interloper and coincident with the asymmetry seen in the X-ray brightness (Figure 2). (ii) A cool ~ 7.5 keV region associated with the southern compact core which is surrounded by hot > 12 keV gas, the hottest of which resides just to the east of the substructure. (iii) A ~ 700 kpc ridge of hot > 11 keV gas running towards the north which separates the northwestern interloper and northern core. (iv) While the northern core and its tail do not appear to have a significantly different temperature to the average temperature, they do appear to be significantly cooler than the regions directly to the west and hotter than the region directly to the east. This is especially clear when considering the tessellated map (middle

left and right panels of Figure 3). (v) The peak in the X-ray surface brightness does not host the coolest gas, as would be expected in a relaxed, cool core cluster.

2.3.2. Pseudo-Entropy, Pseudo-Pressure and Abundance maps

From the non-tessellated temperature map, we have generated projected pseudo-pressure and pseudo-entropy maps, similar to those presented in Finoguenov et al. (2005). These are shown in the bottom left and bottom right panels of Figure 3, respectively. The pseudo-entropy at each pixel is $K = kT_{pix} A_{pix}^{-1/3}$, while the corresponding pseudo-pressure is $P = kT_{pix} A_{pix}^{1/2}$ where A_{pix} is the normalization determined during the fitting of the spectra corrected for exposure and normalized by the area of the extraction region. The northwestern interloper stands out as having the lowest pseudo-entropy in the cluster complex, while the swirl of cool gas, hinted at in the temperature maps, is clearly seen as low entropy gas extending towards the south. The non-hydrostatic nature of Abell 2744 is further highlighted by the asymmetric, patchy pressure distribution which peaks at the X-ray surface brightness peak and has two high pressure fingers trailing off to the southeast and northeast.

Finally, we present an abundance map in the lower left panel of Figure 4. The technique outlined in Section 2.3.1 used to generate the non-tessellated temperature map was again applied. However, the abundance was free to vary during the fitting while, in order to allow more robust abundance determinations, the spectra were extracted from larger regions which contain ~ 3000 counts. The abundances were measured relative to the solar photospheric values of Anders & Grevesse (1989). Included in the top left panel of Figure 4 is the corresponding temperature map which is in broad agreement with the temperature maps presented in the top and middle left panels of Figure 3. The most notable enhancements in abundance seen in the maps presented in the lower panels of Figure 4 are coincident with the southern compact core, the northern core and the northwestern interloper. We identify the northern core as the highest metallicity region within Abell 2744. Furthermore, there is an anticorrelation between the abundance and the temperature inasmuch as the hottest regions also appear to have the lowest abundances.

2.4. Regions of Interest

We now explore the nature of several regions of interest which have been identified from Figures 1, 2 and 3. The selected regions are overlaid onto the temperature and abundance maps in Figure 5. For each region of interest the source spectra, along with the corresponding backgrounds and responses, are extracted and fitted in XSPEC with an absorbed MEKAL model. During the fitting, the column density is fixed to the Galactic value while the temperature, abundance, normalization, and, where the data are of a high enough quality, the redshift are allowed to free to vary during the fit. The best-fitting parameters for each of the regions are presented in Table 2.

2.4.1. Northern Core and Surrounding Structures

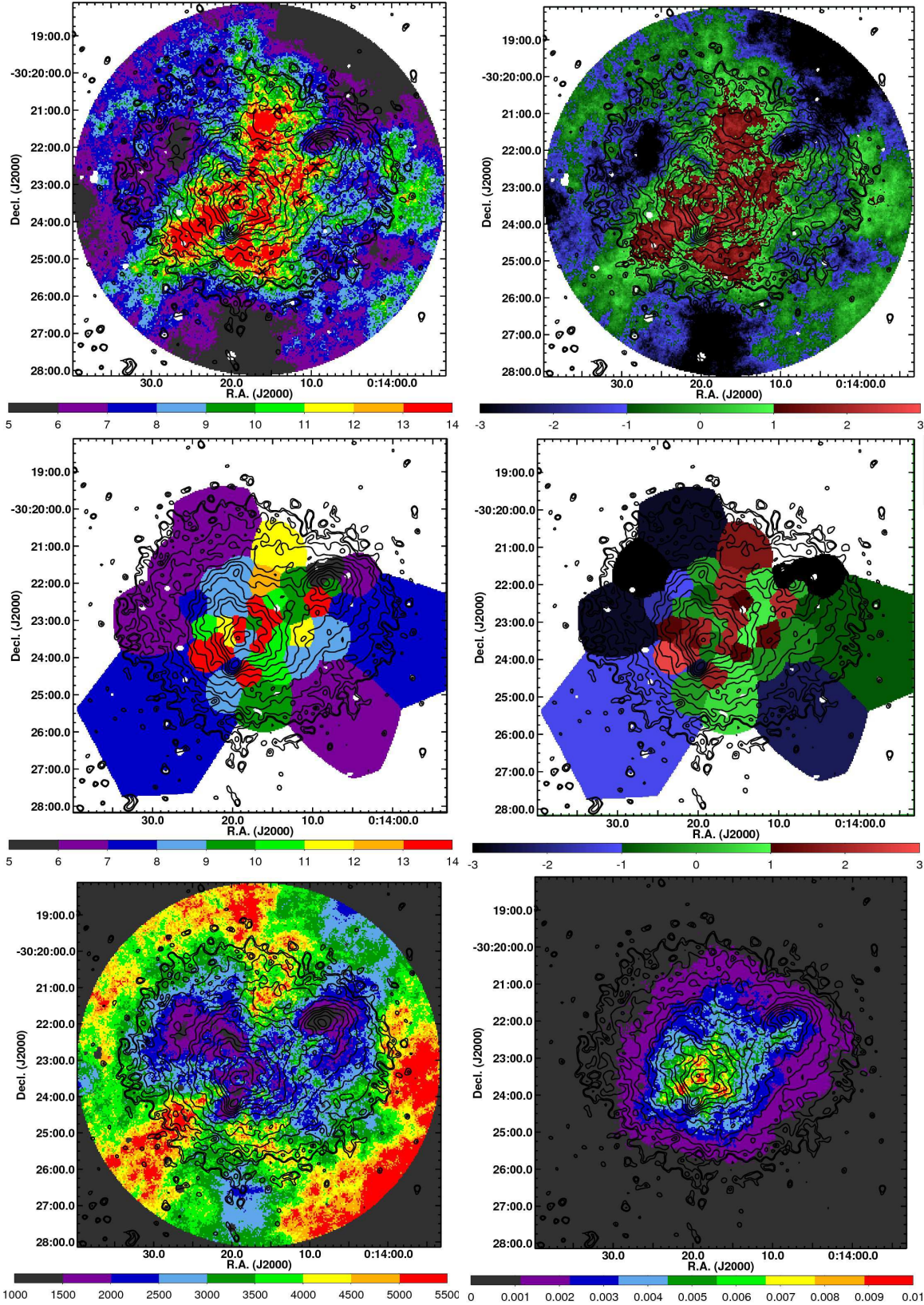


Figure 3. Thermodynamics maps derived from the *Chandra* data. All maps have *Chandra* surface brightness contours overlaid. *Top left:* Temperature map using the method outlined in Randall et al. (2008). The cross points indicate regions where we require a WVT bin to be centered (see text). *Middle left:* Temperature map determined using the WVT binning algorithm to define regions. The color bars on the *top* and *middle left* panels show the temperature scale in keV. *Top and middle right:* Significance of the difference in temperature at each pixel compared to the global temperature where positive (negative) values indicate a higher (lower) temperature. The color bars show the significance scale which has units of the number of σ deviation from the global temperature. *Bottom left and right:* Pseudo-entropy *left* and Pseudo-pressure *right* maps derived from the temperature and normalization. The units of the pseudo-entropy and -pressure maps are arbitrary.

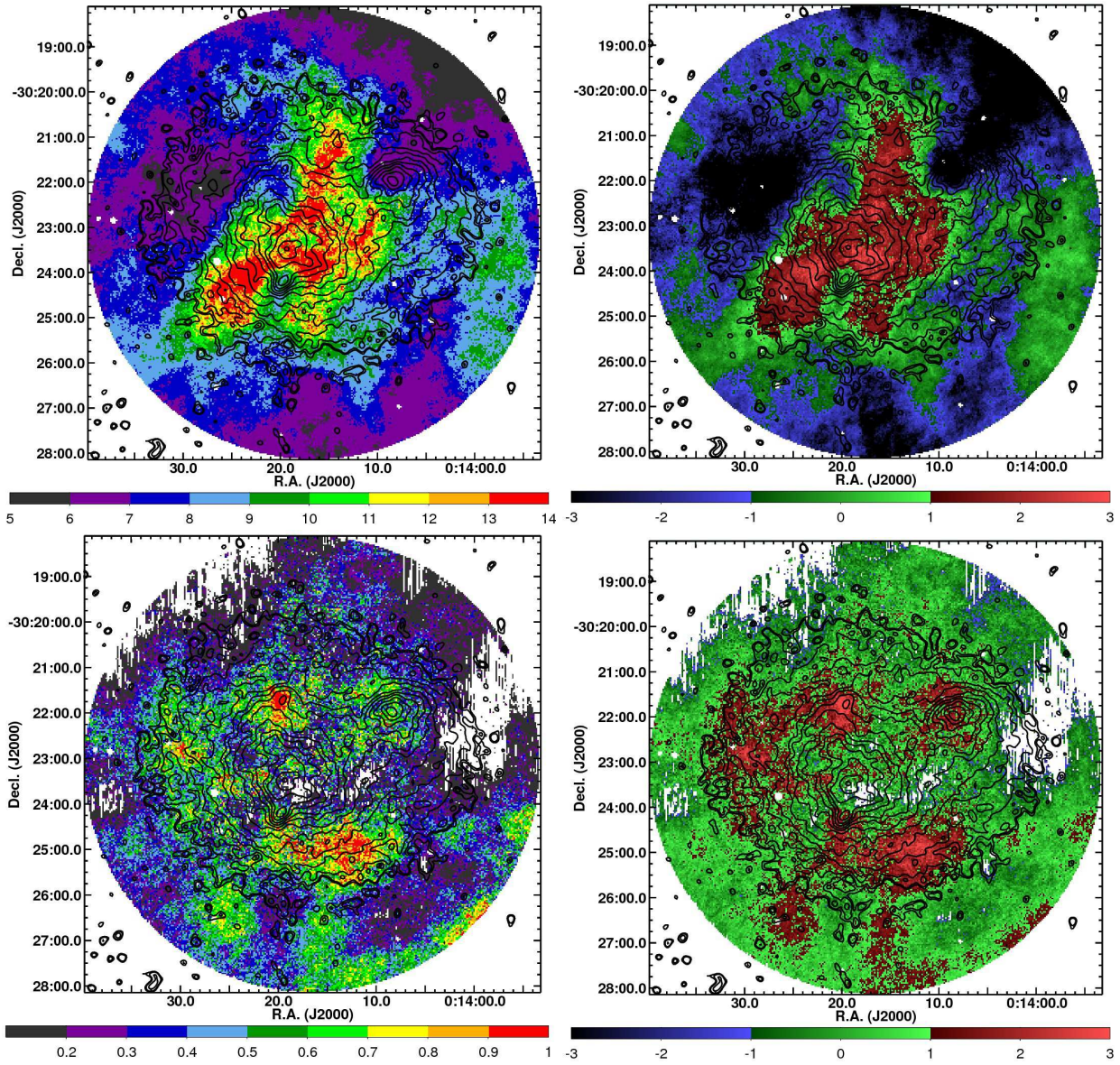


Figure 4. *Top left and right* Same as the *top left and right* panels in Figure 3, but using an extraction region which contains 3000 background subtracted counts and allowing the abundance to vary during the fit. *Bottom left:* The abundance map where the color bar shows the corresponding abundance scale relative to solar. *Bottom right:* The significance of the difference of the abundance at each pixel relative to the global abundance measure. The color bar gives the scale in units of σ .

Table 2
Summary of fits to spectra extracted from the regions of interest.

Region	Description	kT (keV)	Abundance (solar)	z_{gas}	Net Counts
Main Cluster					
R1	central 900kpc	$9.07^{+0.14}_{-0.18}$	$0.262^{+0.026}_{-0.025}$	$0.3033^{+0.0016}_{-0.0030}$	94206
Northern Core Surrounding Structures					
NC1	NC head	$7.36^{+0.75}_{-0.50}$	$0.480^{+0.130}_{-0.126}$	$0.3035^{+0.0087}_{-0.0083}$	3103
NC2	NC Tail	$8.69^{+0.67}_{-0.67}$	$0.424^{+0.125}_{-0.115}$	$0.2846^{+0.0099}_{-0.0129}$	4447
NC3	structure south of NC	$9.05^{+0.92}_{-0.79}$	$0.404^{+0.113}_{-0.132}$	$0.2967^{+0.0068}_{-0.0114}$	2962
Southern Compact Core and Surrounding Structures					
SCC1	SE cool core	$7.70^{+0.97}_{-0.67}$	$0.392^{+0.154}_{-0.139}$	$0.2950^{+0.0088}_{-0.0109}$	2059
SCC2	Outside2 SE cool core	$9.74^{+1.94}_{-1.37}$	$0.329^{+0.234}_{-0.213}$	0.3064	1551
SCC3	Hot reg north of SE cool core	$15.56^{+2.81}_{-1.90}$	$0.0^{+0.152}_{-0.252}$	0.3064	2986
SCC4	Inside edge	$15.83^{+3.80}_{-2.70}$	$0.143^{+0.292}_{-0.267}$	0.3064	1800
SCC5	Outside edge	$8.61^{+1.82}_{-1.42}$	$0.607^{+0.360}_{-0.291}$	0.3064	1260
Northwestern Interloper and Surrounding Structures					
NW1	NW inside front	$6.33^{+0.83}_{-0.70}$	$0.233^{+0.173}_{-0.148}$	$0.3086^{+0.0232}_{-0.0170}$	1270
NW2	NW outside front	$10.45^{+2.52}_{-1.80}$	$0.104^{+0.259}_{-}$	0.3064	1263
NW1	NW inside front deprojected	$5.09^{+0.88}_{-0.71}$	$0.293^{+0.259}_{-0.210}$	$0.3095^{+0.0240}_{-0.0194}$	1270
NW3	NWtail adjacent east	$10.44^{+1.76}_{-1.42}$	$0.300^{+0.207}_{-0.201}$	$0.2935^{0.0159}_{-0.0143}$	1642
NW4	NWtail	$8.12^{+1.10}_{-0.99}$	$0.383^{+0.194}_{-0.168}$	$0.3215^{0.0101}_{-0.0107}$	1686
NW5	NWtail adjacent West	$8.28^{+1.21}_{-1.08}$	$0.000^{+0.144}_{-0.155}$	0.3064	1723
NW4+NW5	Comb NW4 and NW5	$8.34^{+0.83}_{-0.80}$	$0.190^{+0.1146}_{-0.110}$	$0.3189^{+0.0161}_{-0.0119}$	1723+1686
NW6	NWtail adjacent West 2	$11.28^{+3.42}_{-2.37}$	$0.007^{+0.366}_{-0.240}$	0.3064	1635
Miscellaneous Regions					
MISC1	ridge c	$12.46^{+1.55}_{-1.14}$	$0.097^{+0.128}_{-0.119}$	0.3064	4258
MISC2	SB peak	$10.33^{+0.95}_{-0.89}$	$0.215^{+0.101}_{-0.104}$	$0.3189^{+0.0092}_{-0.0110}$	4793
MISC3	Hot ridge north	$13.14^{+2.28}_{-1.85}$	$0.353^{+0.225}_{-0.203}$	$0.2813^{+0.0127}_{-0.0132}$	2470
MISC4	low abundance	$11.46^{+0.82}_{-0.77}$	$0.180^{+0.087}_{-0.090}$	$0.3112^{+0.0067}_{-0.0102}$	7897

The abundance map (bottom left panel of Figure 4) reveals the northern core has significantly higher metallicity than the surrounding gas, while the temperature difference is not significant. Furthermore, both the residual significance and unsharp masked maps (Figure 2) reveal a curved tail of emission trailing to the south of the substructure, as well as a second component ~ 270 kpc to the south. We extract and fit spectra from regions surrounding these structures (NC1, NC2 and NC3 in the right panel of Figure 5). We find that the northern substructure (NC1) does in fact have a significantly lower temperature than the global average, while the NC2 and NC3 regions have temperatures which are consistent with the global average within the quoted confidence levels. Also, we find that at the 68% confidence level all three regions harbor gas with higher abundances than the global value.

2.4.2. Southern Compact Core and Surrounding Structures

There are several regions of interest surrounding the southern compact core including the compact core itself (SCC1 in the left panel of Figure 5) and two hot regions identified in the temperature maps which straddle the core on the northeastern and southwestern sides (SCC2 and SCC3 in the left panel of Figure 5). While the de-

tailed spectra extracted for the SCC2 region reveal the gas there is not significantly hotter than the global average temperature, the region to the northeast (SCC3) does contain significantly hotter gas which also has a very low abundance. We confirm that the southern compact core harbors gas which is both cooler and of a higher abundance than the global averages.

We attempt to quantify the strength of the surface brightness edge just southeast of the southern compact core (Figure 1) by fitting a spherically symmetric broken power law density model centered at the center of curvature of the edge (using the same method as Owers et al. 2009b). The resulting fit gives a jump in density at the edge of $1.60^{+0.15}_{-0.11}$. The surface brightness profile and the best fitting broken powerlaw density model are shown in Figure 6. We note that in ObsIds 7712 and 7915, the chip gap lies very close to the position of the edge. Therefore we repeat the fit using only ObsIds 8477 and 8557. We find that the best fitting surface brightness model gives a density jump of $1.51^{+0.17}_{-0.15}$, consistent with the measurement obtained using the full dataset. The temperature measured just inside the edge (SCC4) is $kT=15.83^{+3.80}_{-2.7}$ keV, while $kT=8.61^{+1.82}_{-1.42}$ keV in the SCC5 region just outside the edge. The change in pressure

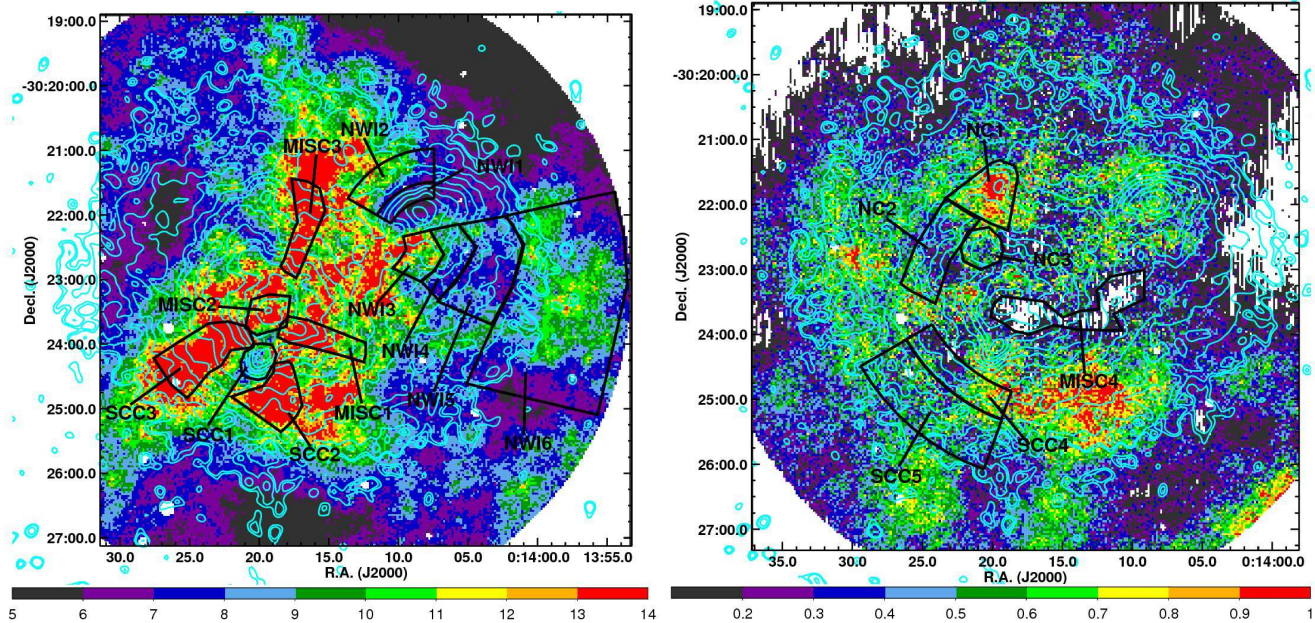


Figure 5. Regions of interest labelled as in Table 2 shown overlaid on the temperature map (*left panel*) and abundance map (*right panel*).

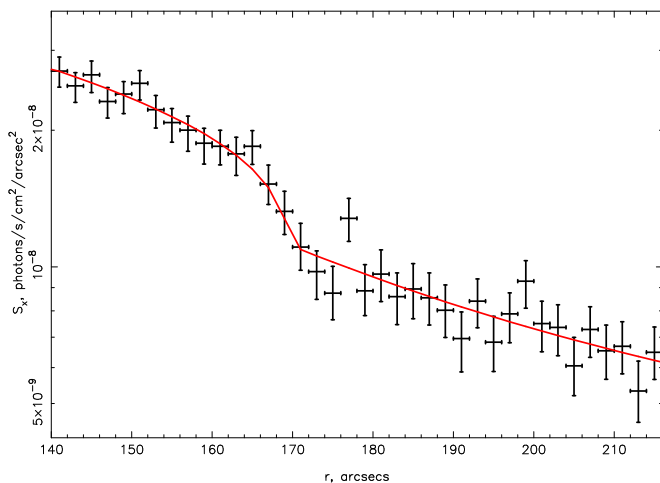


Figure 6. Surface brightness profile across a sector containing the edge to the southeast of the southern compact core (see regions SCC4 and SCC5 in Figure 5). The red curve shows the surface brightness profile for the best fitting broken powerlaw density model.

across this edge is $(n_{e,in}kT_{in})/(n_{e,out}kT_{out}) = 2.94^{+0.98}_{-0.73}$, which indicates a significant pressure jump and thus that the edge is likely a part of a shock front.

2.4.3. Northwestern Interloper and Surrounding Structures

As noted in Section 2.2, the northwestern interloper contains a sharp surface brightness edge to the north. The temperatures just inside and just outside the front (regions NWI1 and NWI2 in the left panel of Figure 5) are $6.33^{+0.83}_{-0.70}$ and $10.45^{+2.52}_{-1.80}$ keV, respectively. Figure 7 shows the surface brightness profile across the edge, which we have fitted with a spherically symmetric broken power law density model centered at the center of curvature of the edge (using the same method as Owers et al. 2009b) with a best fitting density jump of $2.13^{+0.20}_{-0.17}$ (uncertainties are 68% confidence limits). Providing the

geometry assumed in the density model accurately represents the physical geometry of the edge, the temperature just inside the edge will be artificially boosted by hot gas from outside the edge which lies along the line of sight. To account for this, we determine the deprojected temperature inside the edge by including a second MEKAL component in fitting the spectrum extracted from the NWI1 region. This second MEKAL component has temperature, normalizations and abundance frozen to the values determined for the NWI2 region, with the normalizations multiplied by a constant which accounts for the different emission measures due to the different volumes probed (see Owers et al. 2009b, for a detailed explanation of the procedure). The deprojected temperature in the NWI1 region is $5.09^{+0.88}_{-0.71}$ and combining this with the measured density jump and the temperature measured in the NWI2 region, we find that the pressure across the front, given by $(n_{e,in}kT_{in})/(n_{e,out}kT_{out}) = 1.04^{+0.32}_{-0.25}$ is continuous and, thus, the edge is a cold front.

We extract spectra for 4 regions running from east to west across the northwestern interloper's low entropy tail (NWI3, NWI4, NWI5, NWI6 in the left panel of Figure 5). The temperature map (top left panel in Figure 3) indicated that the low entropy tail may harbor cooler gas than the regions immediately to the east and west. Region NWI4 coincides with the lowest projected entropy, while region NWI5 coincides with the lowest temperature gas seen in the temperature maps in the vicinity of the low entropy tail. Regions NWI3 and NWI6 are the regions immediately east and west of the tail, respectively. The temperature and abundance measurements are listed in Table 2 and we find that the temperatures in NWI4 and NWI5 are indeed lower than those measured in NWI3 and NWI6, but only at the 68% confidence level.

2.4.4. Miscellaneous regions with high temperature and/or low abundance.

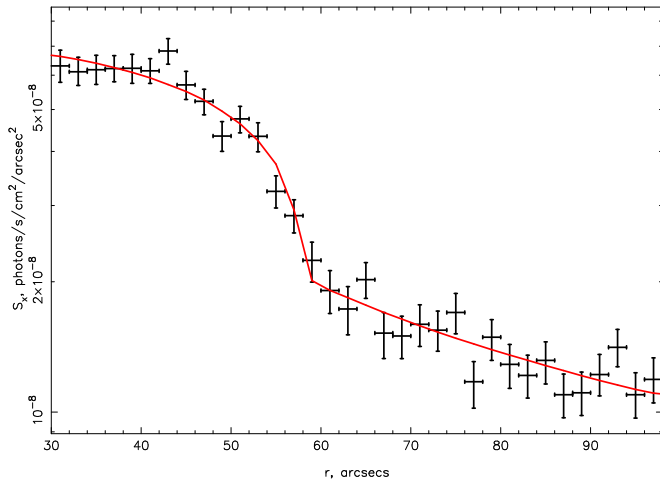


Figure 7. Surface brightness profile across a sector containing the NW substructure cold front (see regions NWI1 and NWI2 in Figure 5). The red curve shows the surface brightness profile for the best fitting broken powerlaw density model.

There are several regions in Figures 5 which have either high temperature (MISC1, MISC2 and MISC3) and and/or an anomalously low abundance (MISC4). The first of the hot regions (MISC1) is roughly coincident with a finger of excess emission clearly seen in the unsharp masked and residual significance images (Figure 2) which extends ~ 450 kpc from the X-ray surface brightness peak and towards the north-northeast (labelled Ridge C in KD04). The second region (MISC2) is coincident with the peak in the X-ray surface brightness while the third region (MISC3) is a streak of hot gas which extends ~ 700 kpc from the peak in the X-ray surface brightness towards the north. We also extract a spectrum for the region which encompasses the low abundance finger running from the peak in the X-ray surface brightness towards the north-northwest (MISC4).

We find that the MISC2 region is marginally hotter than the cluster mean temperature and has an abundance which is statistically consistent with the mean value. The two other regions selected based on their high temperature, MISC1 and MISC3 are both significantly hotter than the mean temperature, consistent with the temperature map results. The abundance of the MISC3 region is consistent, within the uncertainties, with the mean cluster value, while the abundance of the MISC1 region is low when compared to the cluster mean value. The MISC4 region, selected based on its low metallicity, does have a best fitting abundance which is lower than the mean cluster value, but this is not statistically significant.

3. OPTICAL DATA

In this section, we outline the new spectroscopic measurements taken using the AAOmega multiobject spectrograph (MOS) which, when combined with the available redshifts from the literature, provide a sample of 343 spectroscopically confirmed cluster members which we utilize to detect substructures and to constrain the line-of-sight dynamics of the merger.

3.1. Sample selection, Observations and Completeness

Here we outline the selection of galaxies targeted for spectroscopic observations, the observation and reduc-

tion of the spectra, the precision of our redshift measurements and the spectroscopic completeness of our sample.

3.1.1. Photometric Catalog

The primary photometric catalog used for selection of the spectroscopic targets was drawn from the Supercosmos Sky Survey (SSS) server⁵ using the object catalog extraction function. We include only objects within a $15'$ (~ 4 Mpc) radius centered at R.A.= $00^{\text{h}}14^{\text{m}}19^{\text{s}}.5$, decl.= $-30^{\circ}23'19''.0$ (i.e. the center defined by Abell et al. 1989) and brighter than a magnitude of $r_{\text{F}}=21$. We use the SSS classification flag to remove those objects with $r_{\text{F}} < 19$ and not classified as galaxies (the SSS image classification is most reliable for $r_{\text{F}} < 19$ Hamblly et al. 2001) and do not apply any image-classification-based filtering for fainter objects. We cross-match our SSS catalog with the photometric catalog of Busarello et al. (2002) and include those objects which are not detected in the SSS, but appear in the Busarello et al. (2002) catalog and meet our magnitude limit. We exclude a number of objects which are not cluster members based on VLT VIMOS spectroscopy (Filiberto Braglia, priv. comm.; see also Braglia et al. 2009). The resulting catalog contains 1443 targets.

3.1.2. AAOmega Observations

Observations were taken during the nights of 2006 September 12–18 using the AAOmega MOS on the Anglo-Australian Telescope (AAT; Saunders et al. 2004; Smith et al. 2004; Sharp et al. 2006). AAOmega consists of 392 $2''$ diameter fibers available for target allocation across a two degree diameter field of view. During our observations, we used the medium resolution (R 1300) 580V (blue arm) and 385R (red arm) gratings which provide a wavelength coverage of 3700–8800Å and spectral resolutions of 3.5Å and 5.3Å at 4800Å and 7250Å, respectively.

The target density greatly exceeds the maximum fiber packing density, requiring multiple configurations in order to obtain a high level of spectroscopic completeness, particularly in the dense core regions of the cluster. We utilize the simulated annealing algorithm (Miszalski et al. 2006) option within the AAOmega specific *CONFIGURE*⁶ software to generate the fiber allocation files. This software operates most efficiently with an input catalog of $\sim 500 - 800$ objects, particularly when configuring clustered fields. These requirements are met by partitioning the ~ 1500 object primary target catalog into subsamples based on the target magnitude. The magnitude bins used were $r_{\text{F}} < 19.63$, $19.63 < r_{\text{F}} < 20.05$, $20.05 < r_{\text{F}} < 20.37$, $20.37 < r_{\text{F}} < 20.75$ and $20.75 < r_{\text{F}} < 21.00$.

The limiting magnitudes of the subsamples serve two purposes: 1) they allow a fairly random subsampling of the densest regions, thereby reducing the computation time for the *CONFIGURE* software and 2) allow a shorter observation time to reach the desired S/N limit for the brighter subsamples, enabling a more efficient observing strategy. The limits are chosen to allow approximately two configurations per subsample, without under-sampling fiber allocations. The configurations

⁵ See <http://www-wfau.roe.ac.uk/sss/>

⁶ See http://www.aao.gov.au/AAO/2df/aaomega/aaomega_SAconfigure.html

are done in sequence, starting with the brightest magnitude subsample and continuing to fainter subsamples. The unallocated objects in each subsample were propagated through to the next subsample in the configuration sequence. During the fiber configuration process, the *CONFIGURE* software attempts to allocate objects of higher priority ahead of lower priority objects, where prioritization is based on a user-defined rank assigned to each object. We required a high level of spectroscopic completeness in the central regions, so objects within 500kpc of the cluster center were ranked highest. Rankings were decreased as a function of radius in 500kpc radial bins out to a limit of 4Mpc.

This method produced nine configurations and we summarize the observations of these configurations in Table 3. For each configuration, ~ 40 fibers were allocated to blank sky regions for sky subtraction and a further 8 fibers were allocated to bright stars for acquisition and guiding. Differential atmospheric refraction limits the length of contiguous exposures for any one configuration to about three hours, therefore configurations requiring exposures longer than 3 hours were observed across several nights. For each configuration, we took a 5s dome flat and 40s FeAr arc lamp exposures for the purpose of flat fielding and wavelength calibration of the spectra (Note: for configurations observed across several nights, night-specific calibrations were taken). The data were reduced using the AAO *2dFDR* pipeline software⁷ which reduces the red and blue arm data separately, extracting sky subtracted, flat fielded and wavelength calibrated data for each exposure frame. The reduced frames are then co-added (using a weight derived from the total flux in each frame), at which point cosmic rays are identified and rejected. After co-addition, the red and blue-arm spectra are spliced together. At this point, the data were processed using an IDL code which reduces the residuals left from sky subtraction via a Principal Component Analysis (PCA) process which is adapted from software developed by Wild & Hewett (2005, Emily Wisnioski priv. comm. See Drinkwater et al. 2010 for a more detailed explanation).

The reduced, combined, PCA corrected data are then assigned redshifts using the *RUNZ* code, which was written by Will Sutherland for the 2dF Galaxy Redshift Survey (2dFGRS Colless et al. 2001). The *RUNZ* code has been adapted for use with AAOmega spectra and significantly enhanced from its earlier versions. In particular, emission line redshifts measurements have been significantly improved for the WiggleZ survey (Drinkwater et al. 2010). The code measures redshifts using two methods: 1) for absorption line spectra the cross-correlation method of Tonry & Davis (1979) is employed with a suitable library of template spectra, and 2) for emission line galaxies the redshifts are measured for each line by fitting a Gaussian, with the final emission line redshift being determined from the variance weighted mean of the redshifts determined for each emission line. The quality of the assigned redshift was determined by visual inspection and an integer value classification, Q , was assigned, where Q ranges from 1 to 6, using the same scheme adopted for the 2dFGRS, as described in Owers et al. (2009a,c). Briefly, objects with $Q \leq 2$ are assigned no

redshift or an unreliable redshift, objects with $Q = 3, 4$ or 5 have reliable redshifts (with $Q = 5$ having a template-like quality spectrum) and objects with $Q = 6$ are stars or non-extragalactic objects. The AAOmega observations produced reliable ($Q = 3, 4$ or 5) redshifts for 983 extragalactic objects and 276 stars.

3.1.3. Redshift uncertainties

Of the 983 $Q = 3, 4$ or 5 AAOmega observations, there were 38 galaxy spectra with repeat observations. These repeat observations were used to check the uncertainties assigned by *RUNZ* to redshift measurements. We use a robust biweight estimator to determine the mean and dispersion of the distribution of redshift differences, where the redshift measurement with the lower quality (defined by either its lower Q value, or higher error measurement) is subtracted from the higher quality measurement. We find a mean difference of $\overline{\Delta cz} = 1 \pm 13 \text{ km s}^{-1}$ and a dispersion of $87 \pm 21 \text{ km s}^{-1}$ from which we can infer a single redshift measurement uncertainty of $61 \pm 15 \text{ km s}^{-1}$. The median value of the individual redshift uncertainties assigned by *RUNZ* to non-stellar objects was 66 km s^{-1} (after excluding 6 outliers with error values greater than 1000 km s^{-1}), which is consistent with the uncertainty derived from the repeat observations.

Independent checks on the redshifts and their uncertainties can be made by cross-correlating the AAOmega catalog with the Couch & Sharples (1987), Couch et al. (1998), Boschin et al. (2006) and Braglia et al. (2009) redshift catalogs. Further to these catalogs, we add archival 2dF data, which is reduced using 2dFDR and redshifted using the RVSAO package in IRAF (Kurtz & Mink 1998). The results of the comparisons are presented in Table 4 where the columns are: Origin of external redshift catalog for comparison (Col. 1); number of redshifts in common with the AAOmega catalog, N_{match} , where catalog members are deemed to be matches if their positions differ by less than $3''$ (Col. 2), the mean redshift difference, $\overline{\Delta cz} = \overline{cz_{\text{ours}} - cz_{\text{ext.}}}$, as determined by the biweight estimator (Col. 3), the dispersion in the Δcz distribution, $\sigma(\Delta cz)$, determined with the biweight estimator (Col. 4), the redshift uncertainty for the external redshift measurements (Col. 5), the quadrature difference between $\sigma(\Delta cz)$ and the external redshift error which gives an external estimate of the uncertainty on the AAOmega measurements (Col. 6) and the ratio of the external uncertainty measurement to the internal uncertainty measurement derived above (Col. 7). We note that the results in Table 4 show our internal redshift uncertainties are systematically underestimated by a factor of ~ 1.8 . We conclude that the redshift precision of the AAOmega measurements are $\sim 110 \text{ km s}^{-1}$.

3.1.4. Combined Redshift Catalog

As can be seen from Table 4, there are significant offsets from a mean of zero for all of the Δcz distributions, aside from the comparison with the Boschin et al. results. In order to ensure the external redshift measurements are consistent with the AAOmega ones, prior to combining the catalogs we add the pertinent value of $\overline{\Delta cz}$ to each redshift measurement in the Braglia et al., Couch et al. and Couch & Sharples catalogs. When combining the catalog, for consistency we always use AAOmega

⁷ See http://www.aao.gov.au/AAO/2df/aaomega/aaomega_software.html#2dfr

Table 3
Summary of the AAOmega observations.

Field	Date	r_F Limit	T_{exp}	$N_{objects}$	$N_{Redshift}$	Seeing
1	2006 Sep 12	19.63	$5 \times 1800s$	192	180	$1''.2$
2	2006 Sep 13, 14	19.63	$4 \times 1800 + 3 \times 1800s$	134	126	$1''.4$
3	2006 Sep 12	20.05	$10 \times 1800s$	172	161	$1.2-1''.4$
4	2006 Sep 13, 14, 15	20.37	$4 \times 1800 + 6 \times 1800 + 5 \times 1800s$	181	147	$1.0-1''.5$
5	2006 Sep 13, 14, 15	20.37	$1 \times 1800 + 5 \times 1800 + 4 \times 1800s$	130	114	$1.0-1''.5$
6	2006 Sep 15, 16	20.75	$5 \times 1800 + 7 \times 1800s$	190	152	$1.0-1''.5$
7	2006 Sep 16, 17	20.75	$5 \times 1800 + 5 \times 1800s$	133	109	$1''.0$
8	2006 Sep 17, 18	21.00	$(10 \times 1800 + 1 \times 1200) + (6 \times 1200 + 1 \times 800)s$	191	157	$1''.0$
9	2006 Sep 18	21.00	$(12 \times 1800)s$	149	113	$1''.0$

Table 4
Comparison of AAOmega redshift measurements with literature values. The errors presented for $\overline{\Delta cz}$ and $\sigma(\Delta cz)$ are determined from the 68% confidence limits based on 10000 bootstrap resamplings of the data.

Literature source	N_{match}	$\overline{\Delta cz}$ km s^{-1}	$\sigma(\Delta cz)$	Literature redshift uncertainty km s^{-1}	Quadrature difference km s^{-1}	ratio km s^{-1}
Braglia et al. (2009)	60	88^{+39}_{-38}	289^{+46}_{-40}	276	86 ± 156	1.4 ± 2.6
Boschin et al. (2006)	56	-18^{+23}_{-24}	172^{+19}_{-18}	90	147 ± 22	2.4 ± 0.7
Couch et al. (1998)	29	177^{+24}_{-24}	125^{+23}_{-18}	90	87 ± 32	1.4 ± 0.6
Couch & Sharples (1987)	28	-89^{+27}_{-27}	151^{+24}_{-26}	100	113 ± 32	1.5 ± 0.7
2df 2003	24	-53^{+27}_{-26}	136^{+20}_{-23}	50	127 ± 21	2.1 ± 0.6

redshifts where an object has multiple redshift measurements. Where an object has multiple AAOmega measurements, we choose the measurement with the highest Q value, and where the Q values are equal, we choose the measurement with the lower redshift uncertainty. Our final combined catalog contains 1237 extragalactic objects with robust redshift measurements within a $15'$ radius of the cluster. The position, r_F magnitude, redshift, redshift uncertainty and redshift source for all galactic and extragalactic objects in our catalog are tabulated in Table 5.

3.1.5. Spectroscopic Completeness

In the forthcoming sections, we will use the redshift catalog to search for substructure in Abell 2744. Therefore, in order to be confident in the results, it is important that the spectroscopic completeness is well understood, particularly for the interpretation of maps of the projected density of the member galaxies. We use the combined redshift catalog to determine the spectroscopic completeness, which is defined as the ratio of the number of objects with reliable redshift determinations to the number of objects in the parent photometric catalog. In Figure 8 we present the spectroscopic completeness as a function of radius, r_F magnitude and a combination of radius and r_F magnitude. The plots show that we have obtained a high level of completeness at all cluster-centric radii and for all magnitude ranges. However, the spectroscopic completeness is systematically lower within the central ~ 1 Mpc (although we note it is still excellent and remains above $\sim 70\%$ for all magnitude ranges). This is due to a combination of fiber separation limits ($\sim 30''$) and the high galaxy surface density in the central regions, which means a small number of objects could not be observed.

Figure 9 shows two images of the spatial distribution of the spectroscopic completeness for the magnitude limits $r_F < 20.5$ (left panel) and $r_F < 21$ (right panel). The images were generated by first producing an adaptively binned image of the spatial distribution of the galaxies in the photometric catalog where each spatial bin contains ~ 10 galaxies. We made use of the WVT binning algorithm by Diehl & Statler (2006), which is a generalization of Cappellari & Copin (2003)'s Voronoi binning algorithm. The same spatial binning was then applied to the galaxies in the spectroscopic catalog to produce a second image. The ratio of the binned spectroscopic to photometric images gives the spectroscopic completeness map in Figure 9. The maps reveal the high level of spectroscopic completeness we have obtained with our observations and, in particular, for $r_F < 20.5$ we obtain $\gtrsim 90\%$ completeness over the majority of the 6 Mpc diameter field. For $r_F < 21$ we obtain $\gtrsim 80\%$ completeness over the majority of the 6 Mpc diameter field. The systematically lower spectral completeness within 1 Mpc noted in the radial profile shown in the right panel of Figure 8 is due to a region of low completeness confined to the north west of the center. This patch of lower spectral completeness needs to be kept in mind in the forthcoming sections.

3.1.6. Cluster Membership

Robustly distinguishing cluster members from foreground and background interlopers is a critical first-step when conducting a dynamical analysis. Membership allocation is a two-step process where the initial step involves crudely separating cluster members and projected interlopers in redshift-space only. This is achieved by selecting galaxies within the redshift window of $cz_{clus} \pm 10000 \text{ km s}^{-1}$ (where $z_{clus} = 0.306$; Boschin et al. 2006)

Table 5
Combined redshift catalog.

R.A. (J2000) deg.	decl. (J2000) deg.	r_F magnitude	(cz) km s^{-1}	cz uncertainty km s^{-1}	cz Quality	cz source
3.296875	-30.391694	20.69	400971.27	314.78	4	AAT/AAOmega
3.303542	-30.358722	19.62	99.13	113.92	6	AAT/AAOmega
3.303875	-30.404806	20.55	56010.02	20.99	5	AAT/AAOmega
3.304125	-30.367528	19.47	234.52	65.95	6	AAT/AAOmega
3.305000	-30.431861	20.75	103.98	65.95	6	AAT/AAOmega
3.305750	-30.351361	20.48	28873.99	20.99	3	AAT/AAOmega
3.305833	-30.339167	20.27	92533.37	23.98	5	AAT/AAOmega
3.306250	-30.380945	22.20	63794.34	276.00	3	Braglia et al. (2009)
3.308583	-30.363083	19.57	78171.58	23.98	5	AAT/AAOmega
3.310292	-30.324250	19.25	93436.37	74.95	4	AAT/AAOmega
3.313542	-30.398889	18.91	91532.63	23.98	5	AAT/AAOmega
3.314292	-30.344611	18.90	92477.01	113.92	4	AAT/AAOmega
3.313542	-30.398889	18.91	91532.63	23.98	5	AAT/AAOmega
3.314292	-30.344611	18.90	92477.01	113.92	4	AAT/AAOmega
3.314583	-30.472861	19.14	92390.06	86.94	4	AAT/AAOmega

Note. — This table is available in its entirety in a machine-readable form in the online journal. A portion is shown here for guidance regarding its form and content.

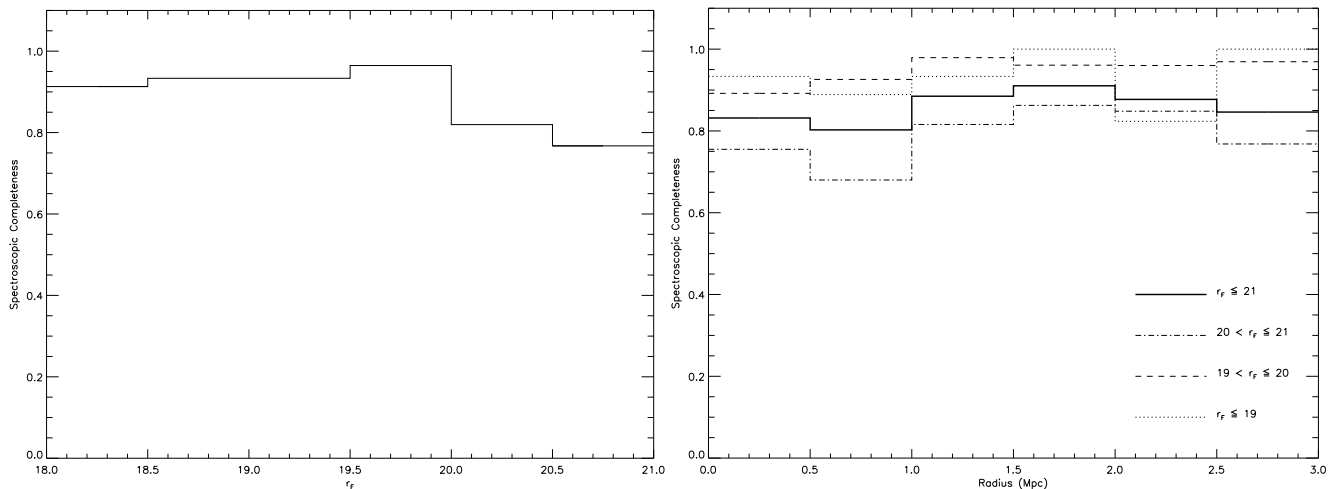


Figure 8. Spectroscopic completeness as a function of magnitude (left) and as a function of radius (right). Also plotted in the right panel is the spectroscopic completeness as a function of radius for the magnitude ranges indicated at the lower right of the figure.

which, as the left panel in Figure 10 shows, defines a peak in redshift space associated with Abell 2744. The second part of the process refines the membership allocation by using a slightly modified version of the “shifting gapper” first employed by Fadda et al. (1996). This method utilizes both radial and peculiar velocity information to separate interlopers from members as a function of cluster-centric radius (defined with respect to the bright cluster galaxy [BCG] closest to the X-ray peak at R.A.=00^h14^m20^s.738, decl.=−30°23′59″.90) and is described in detail in Owers et al. (2009c). Briefly, the data are binned radially such that each bin contains at least 40 objects. Within each bin galaxies are sorted by their peculiar velocity and interlopers are rejected based on the size of the gap in velocity between adjacent (in peculiar velocity) objects. The limit of 40 objects per bin is somewhat subjective and is chosen to minimize both the radial annulus used and the likelihood of the algorithm rejecting either high velocity bona fide cluster members or coherent substructures associated with merger activity. Binning by 40 objects produces the best results, as

shown in the right panel of Figure 10 where we present the results of the shifting gapper membership allocation procedure. Figure 10 shows that within a cluster-centric radius of 3 Mpc the cluster members are well separated from the surrounding interlopers. Beyond 3 Mpc the separation is less-clear, so we exclude the galaxies at these larger radii during the analysis. After culling the interlopers, 343 bona fide cluster members remain from which we determine a cluster redshift of $z_{clus} = 0.3064 \pm 0.0004$ and a velocity dispersion of $\sigma_{clus} = 1497 \pm 57 \text{ km s}^{-1}$ using biweight estimators of location and scale (Beers et al. 1990), where the quoted errors are 1σ values determined using the jackknife resampling technique.

Also plotted in the right panel of Figure 10 are the means (filled circles) and 3σ limits (filled diamonds) for each radial bin, determined using biweight estimators, showing that all excluded interlopers have peculiar velocities exceeding the 3σ limit at the radial bin of interest. The inadequacy of a simple 3σ clipping using only velocity information is highlighted in the right panel of Figure 10, where the dashed-lines show that the $3\sigma_{clus}$

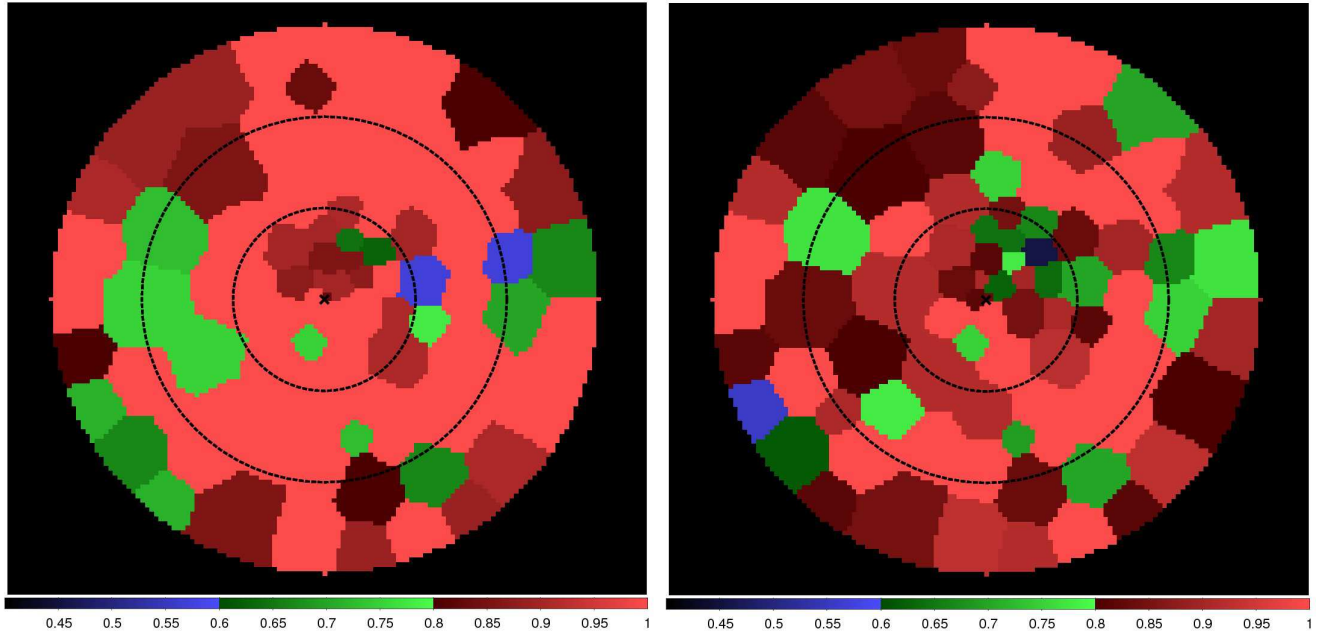


Figure 9. Left panel: Spectroscopic completeness map for $r_F < 20.5$. Right panel: Spectroscopic completeness map for $r_F < 21$. The black dashed circles have radii 1 and 2 Mpc while the black cross marks the position of the BCG.

limits fail to reject several interlopers at larger cluster-centric radii.

4. SUBSTRUCTURE DETECTION

The primary motivation for this paper is to detect and characterize substructure in order to understand the merger history of Abell 2744. While substructure tests that use all available information (position on the sky and the line of sight velocity) are more decisive (Dressler & Shectman 1988; West & Bothun 1990; Pinkney et al. 1996; Burgett et al. 2004), the results of simpler analyses are easier to comprehend. In this section, we begin with a one-dimensional analysis of the velocity distribution, which is most sensitive to detecting substructure caused by line-of-sight mergers where the velocity difference is large. We then search for substructure in the two-dimensional galaxy distribution, which is most sensitive to detecting well-separated mergers occurring in the plane of the sky. Finally, we combine the spatial and velocity information to search for local deviations from the global velocity distribution which indicate dynamical substructures.

4.1. Substructure in the Velocity Distribution

Cluster mergers can induce significant distortions in the observed velocity distribution which, when a cluster is dynamically relaxed, is well approximated by a Gaussian. Therefore, searching for evidence of substructure using velocity information is generally accomplished by testing for departures from a Gaussian shape. Here, we use the method first outlined by Zabludoff et al. (1993) which approximates the velocity distribution by the summation of three Gauss-Hermite functions. The method is described in detail in Owers et al. (2009c). The coefficient of the first term, $h_0 \approx 1$, multiplies the best-fitting Gaussian contribution to the distribution while the second and third terms, with coefficients h_3 and h_4 , approximate the third- and fourth-order asymmetric and

symmetric deviations from a Gaussian shape, similar to skewness and kurtosis measurements but less sensitive to outliers in the distribution. For Abell 2744, we find the coefficients have values of $h_3 = 0.07$ and $h_4 = 0.06$. The significance of these values is determined by generating 10,000 Monte Carlo realizations of Gaussians with $N = 343$ data points having mean and standard deviation equal to the best-fitting value derived from the data. We find that values of $|h_3| > 0.07$ occur in only 6% of the realizations, while values of $|h_4| > 0.06$ occur 8% of the time. Thus, there appear to be mildly significant symmetric and asymmetric deviations from Gaussianity present in Abell 2744’s velocity distribution.

The positive value for the h_4 term is likely to be due to the contribution of galaxies in the cluster outskirts, which follow more radial orbits and hence produce a more peaked velocity distribution (Merritt 1987), rather than the presence of substructure. Because we are interested in detecting structure related to a cluster merger and not due to orbital anisotropy, we re-determine the Gauss-Hermite coefficients using only data from the central 1.5 Mpc region. There are 238 galaxies within this region in our sample and for these we measure $h_3 = 0.12$ and $h_4 = -0.03$. The observed h_3 coefficient is highly significant with $|h_3| > 0.12$ occurring in less than 1% of the realizations, while the h_4 term is not significant and $|h_4| > 0.03$ occurs in 47% of the realizations, verifying that the mildly significant positive h_4 value measured above is indeed due to the contribution of the galaxies at larger cluster-centric radii.

As noted previously, the velocity distribution in Abell 2744 is bi-modal (Girardi & Mezzetti 2001; Boschin et al. 2006; Braglia et al. 2007). This bi-modality causes the significantly positive h_3 term and Figure 11 clearly shows a secondary substructure with a peak at $v_{pec} \sim 2000 \text{ km s}^{-1}$. To further quantify the significance of this bi-modality, we use the KMM algorithm (Kaye’s

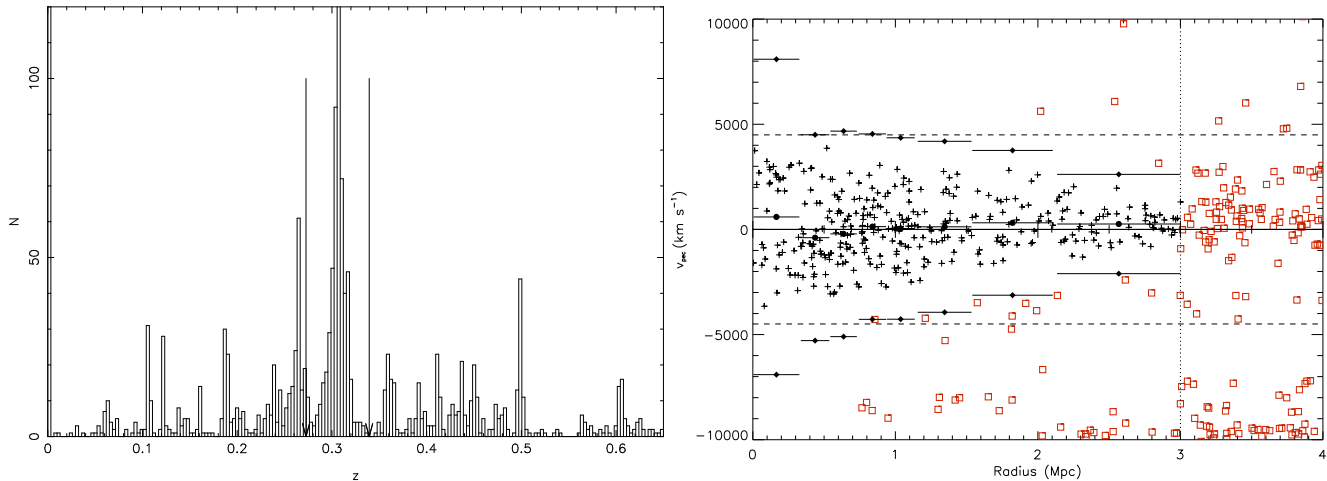


Figure 10. *Left panel:* A histogram of all the reliable redshifts measured within the Abell 2744 field. Arrows mark the initial cut in velocity used to crudely isolate the cluster in redshift-space. *Right panel:* Shift gapper plot for refined member allocation. The *black* crosses represent galaxies allocated as cluster members while the *orange* open squares are rejected foreground and background galaxies lying close to the cluster in redshift space.

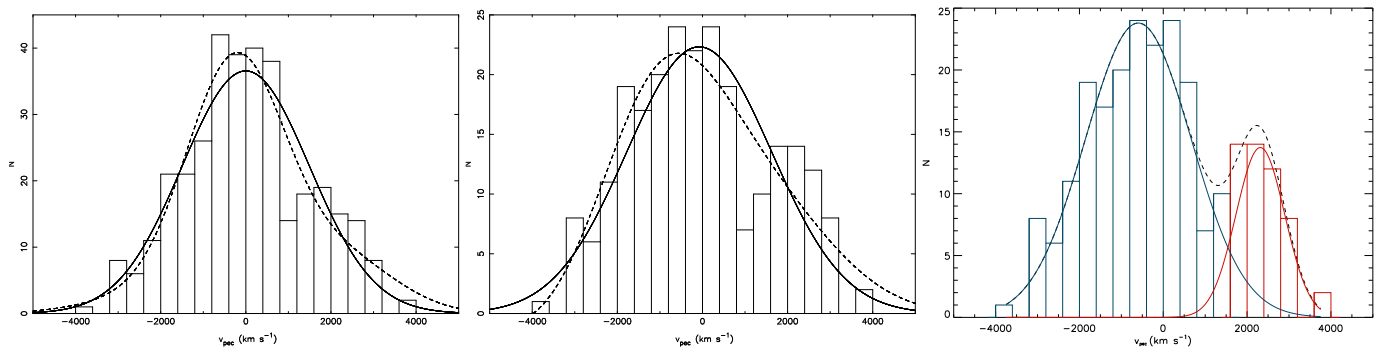


Figure 11. *Left panel:* Peculiar velocity histogram for all 343 members. The solid line shows a Gaussian with $\overline{v_{pec}} = 0 \text{ km/s}$ and $\sigma = 1497 \text{ km s}^{-1}$ and the dashed-line shows the Gauss-Hermite reconstruction of the velocity distribution. *Middle panel:* Same as the *left panel* for the 238 members within a 1.5 Mpc radius of the cluster center. Here, the plotted Gaussian (solid line) has $\sigma = 1701 \text{ km s}^{-1}$. *Right panel:* The results of the KMM partition for the members within 1.5 Mpc. The blue Gaussian has $\overline{v_{pec}} = -596 \text{ km/s}$ and $\sigma = 1261 \text{ km s}^{-1}$ and the red Gaussian has $\overline{v_{pec}} = 2316 \text{ km/s}$ and $\sigma = 581 \text{ km s}^{-1}$. The dashed line shows the combined red and blue Gaussians.

Mixture Model; Ashman et al. 1994) to fit two Gaussians to the velocity distribution of the members residing within a cluster-centric radius of 1.5 Mpc. As input for the main component, we set a mean $\mu_{1,init} = 0$, dispersion $\sigma_{1,init} = 1300 \text{ km s}^{-1}$ and estimate the fractional contribution of the number of galaxies belonging to the main component with respect to the entire distribution is $f_{1,init} = 0.7$. Likewise, for the secondary component we set $\mu_{2,init} = 2000 \text{ km s}^{-1}$, $\sigma_{2,init} = 500 \text{ km s}^{-1}$ and $f_{2,init} = 0.3$. As output, the algorithm returns $\mu_{1,out} = -596 \text{ km s}^{-1}$, $\sigma_{1,out} = 1261 \text{ km s}^{-1}$ and $f_{1,out} = 0.79$ for the main component and $\mu_{2,out} = 2316 \text{ km s}^{-1}$, $\sigma_{2,out} = 581 \text{ km s}^{-1}$ and $f_{2,out} = 0.21$ for the secondary component. It is noted that the outputs generated by the KMM algorithm are robust to changes in the initial input parameters. The resulting Gaussians are overplotted on the observed velocity distribution in right panel of Figure 11. Since we are using the algorithm for a heteroscedastic (i.e., where the variances differ) case, the estimate of the significance of the likelihood ratio test statistic (LRTS) comparing a bi-modal fit to the null-hypothesis uni-modal fit given by the algorithm is unre-

liable (Ashman et al. 1994). To reliably determine the significance of the LRTS, we produce 10,000 randomly sampled Gaussian distributions with 238 data points, mean -38 km s^{-1} and dispersion 1632 km s^{-1} (i.e., mean and standard deviation which best describes the observed velocity distribution). For each random dataset, two Gaussians are fitted using the KMM algorithm, as was done for the observations, where the initial inputs are set to the best-fitting outputs for the observed velocity distribution listed above and the LRTS is computed. Comparison of the observed LRTS to the distribution of 10,000 LRTS produced by the random uni-modal Gaussian datasets allows the significance of the observed LRTS to be reliably determined. The observed LRTS is larger than 99.99% of the LRTSs produced in the 10,000 realizations and we conclude that a bi-modal fit is significantly better than a uni-modal one.

4.2. Substructure in the Spatial Distribution of Member Galaxies

Having shown that the velocity distribution in Abell 2744 is bi-modal, we now search for further evidence of merger-related substructure using 2D spatial

information. To that end, we have used the positions of the 343 spectroscopically confirmed members to produce maps of the smoothed galaxy surface density (Figure 12). We used a variable width Gaussian smoothing, where the width, σ , at each pixel is the projected distance to the tenth nearest galaxy, limited to a minimum of 90 kpc and a maximum of 500 kpc in high and low density regions, respectively. As detected previously (Boschin et al. 2006; Braglia et al. 2009), two distinct substructures inhabit the central regions of the cluster—the most significant one is centered close the cluster center (which was arbitrarily defined in Section 3.1.6 to be the position of the BCG nearest the peak in the X-ray surface brightness) and a second substructure ~ 600 kpc to the north. At larger scales the distribution of galaxies appears smooth, apart from a structure ~ 2.5 Mpc to the west and a mild asymmetry to the north-west.

Given the bimodality detected in the velocity distribution, we search for any correlation between the two velocity peaks and the two substructures seen in the 2D galaxy density map for the spectroscopically confirmed members (top panels of Figure 12). To achieve this, we plot separately the spatial distributions of the galaxies allocated to the two KMM velocity partitions in Section 4.1 and smooth the resulting distributions with an adaptive circular top hat filter with radius set such that the smoothing region contains 10 galaxies. These plots are shown in Figure 13 where the left and right panels show the distributions of galaxies assigned to the lower and higher velocity partition, respectively. The spatial distribution of the galaxies assigned to the dominant (both in terms of number of galaxies and velocity dispersion) lower velocity partition has two local peaks in galaxy surface density. The most significant of these two peaks is located coincident with the northern substructure seen in Figure 12, while the less significant one is approximately coincident with the more central density peak seen in Figure 12. The spatial distribution of the high velocity partition also has its peak density approximately coincident with the central density peak seen in Figure 12. This indicates that the density peak seen close to the center in Figure 12 is not the center of the cluster, but is caused by the alignment of two substructures separated by a large velocity and projected along our line of sight.

Inspecting the completeness map Figure 9 reveals that galaxies in the region of the northern peak are under-represented in our spectroscopic sample. Presumably, improving the sample completeness in this region would enhance the local density peak. Thus the northern peak is likely to be even more significant than it appears to be in Figure 13.

The top right panel in Figure 12 shows a close up of the smoothed member galaxy surface density in the central 1×1 Mpc region with *Chandra* X-ray contours overplotted. Neither of the local peaks in galaxy surface density coincides with a peak in X-ray surface brightness. Of particular concern is the lack of any significant overdensity coincident with the northwestern interloper where Boschin et al. (2006) and Braglia et al. (2009) both detected substructure using photometrically selected cluster members. As noted in Section 3.1.5, the region just northwest of the center has the lowest spectroscopic completeness and this may be a contribut-

ing factor in the non-detection of substructure in this region. To test this, we obtain the photometric catalog⁸ of Busarello et al. (2002), which covers the central 2.3×2.3 Mpc region, and utilize their publicly available photometric redshifts to define cluster membership as per the definition in Busarello et al. (2002). The lower left panel of Figure 12 shows the adaptively smoothed galaxy surface density for the photometric members with $R \leq 21$ (where $70 \leq \sigma \leq 400$ kpc). At this magnitude limit, which approximately matches our spectroscopic limit of $r_F=21$, there is qualitative agreement with the structures detected in the galaxy surface density map for the spectroscopically confirmed members. Therefore, the non-detection of a significant local overdensity coincident with the northwestern interloper, as detected by Boschin et al. (2006) and Braglia et al. (2009), is not due to the lower spectroscopic completeness, but rather is due to the fact that the majority of the galaxies contributing to the overdensity there are fainter than our limiting magnitude. This can be seen in the lower right panel of Figure 12 where we have plotted the adaptively smoothed galaxy surface density for the photometric members down to the completeness limit of $R = 22.3$ (where $50 \leq \sigma \leq 400$ kpc). This map reveals the presence of an overdensity approximately coincident with the northwestern interloper, consistent with the maps of Boschin et al. (2006) and Braglia et al. (2009). This result is consistent with Andreon (2001) who, using deep *K*-band imagery, find significantly more dwarf galaxies and significantly fewer bright galaxies in this northwestern region when compared to the central cluster region (which is roughly coincident with our defined cluster center). Confirmation that this overdensity is part of the Abell 2744 system requires deeper spectroscopic observations.

4.3. Substructure from 3D spatial plus velocity information

We now combine the spatial and velocity information to determine if there is any correlation between the substructures detected in the 2D spatial and 1D velocity distributions above. This is achieved by making use of the κ -test which was successfully employed by Colless & Dunn (1996) to detect substructure in the Coma cluster. The κ -test searches for local departures from the global velocity distribution around each cluster member galaxy. This is accomplished by using the Kolmogorov-Smirnov (KS) test which determines the likelihood that the velocity distribution of the $n = \sqrt{N}$ (where N is the number of cluster members) nearest neighbors around the galaxy of interest and the global cluster velocity distribution, which includes the remaining $N - n$ galaxies, are drawn from the same parent distribution. The likelihood is determined by measuring the maximum separation of the two cumulative distribution functions, D_{obs} and determining the probability that the D -statistic is larger than D_{obs} for the given sample sizes, $P_{KS}(D > D_{obs})$. The global measure of the dynamical substructure present within the cluster, κ , is determined by summing the negative log-likelihood for each galaxy over the entire sam-

⁸ <http://vizier.cfa.harvard.edu/viz-bin/VizieR?source=J/A+A/389/787/>

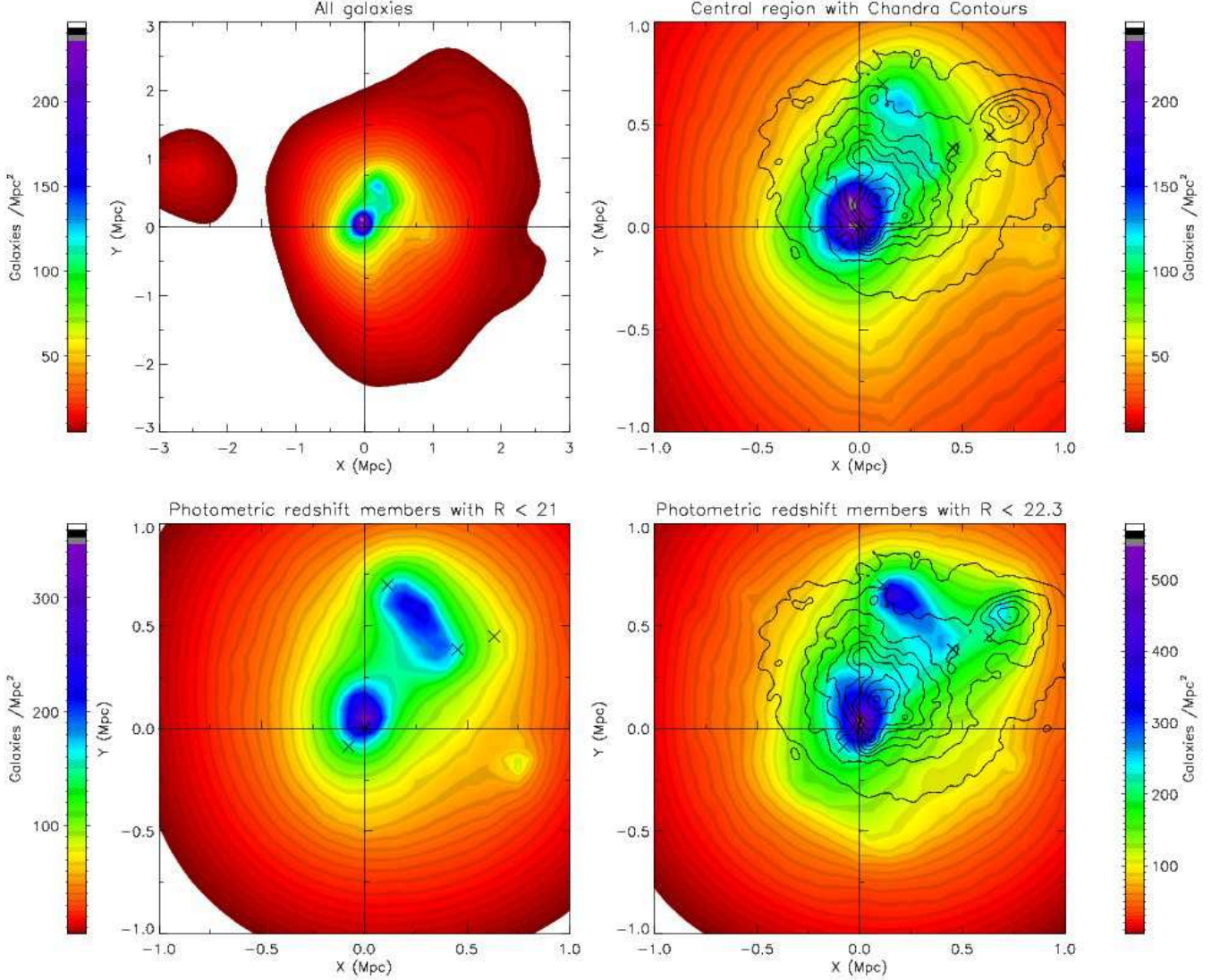


Figure 12. *Top left panel:* This panel shows the adaptively smoothed galaxy surface density distribution for all spectroscopically confirmed cluster members. *Top right panel:* Close-up of the image in the *Top left panel* with *Chandra* isointensity contours overlaid. Crosses mark the positions of the 5 bright cluster members. *Bottom left panel:* Adaptively smoothed galaxy surface density for photometrically defined cluster members with magnitudes brighter than $R=21$ (see text). *Bottom right panel:* Same as *Bottom left panel* but for galaxies brighter than $R=22.3$. Note the emergence of a substructure coincident with the X-ray substructure revealed by the *Chandra* contours. In all panels, the color bars show the projected galaxy surface density scale in units of galaxies/Mpc².

ple, i.e.

$$\kappa = \sum -\log P_{KS}(D > D_{obs}). \quad (2)$$

The significance of κ is determined by performing 10,000 Monte Carlo realizations where, for each realization, the observed positions of the galaxies are retained, while the galaxy velocities are shuffled randomly, removing any correlation between positions and velocities. The observed κ value is then compared to the distribution of the 10,000 Monte Carlo realizations of κ . A value as high as the observed value of $\kappa = 481$ does not occur in the 10,000 realizations, which have a distribution that is well modeled by a log-normal distribution with $\mu(\ln \kappa) = 4.95$ and $\sigma(\ln \kappa) = 0.19$. Thus, the observed κ value lies $\sim 6.6\sigma$ from the mean of the realizations and the upper limit on the probability of observing a value this high by chance is 10^{-4} .

Figure 14 shows the results of the κ -test in the form of

a “bubble plot.” At the position of each member galaxy, a circle is plotted with radius $\propto -\log P_{KS}(D > D_{obs})$. Clusters of large bubbles reveal regions where the local dynamics are different from the global cluster dynamics; we define significantly large bubbles as those with radii that occur in less than 1% of the 10,000 realizations and these are emboldened in Figure 14. The bubbles are also color-coded based on the sign of the galaxy’s peculiar velocity, where red and blue mark positive and negative v_{pec} , respectively. Overplotted are the galaxy surface density contours taken from the adaptively smoothed image shown in the top left panel of Figure 12. There are two clear dynamical substructures detected in the central ~ 1 Mpc; one coincident with the cluster center and another to the north, coincident with the second projected galaxy overdensity. At larger radii, we also detect the two substructures to the northwest and south first noted by Braglia et al. (2007).

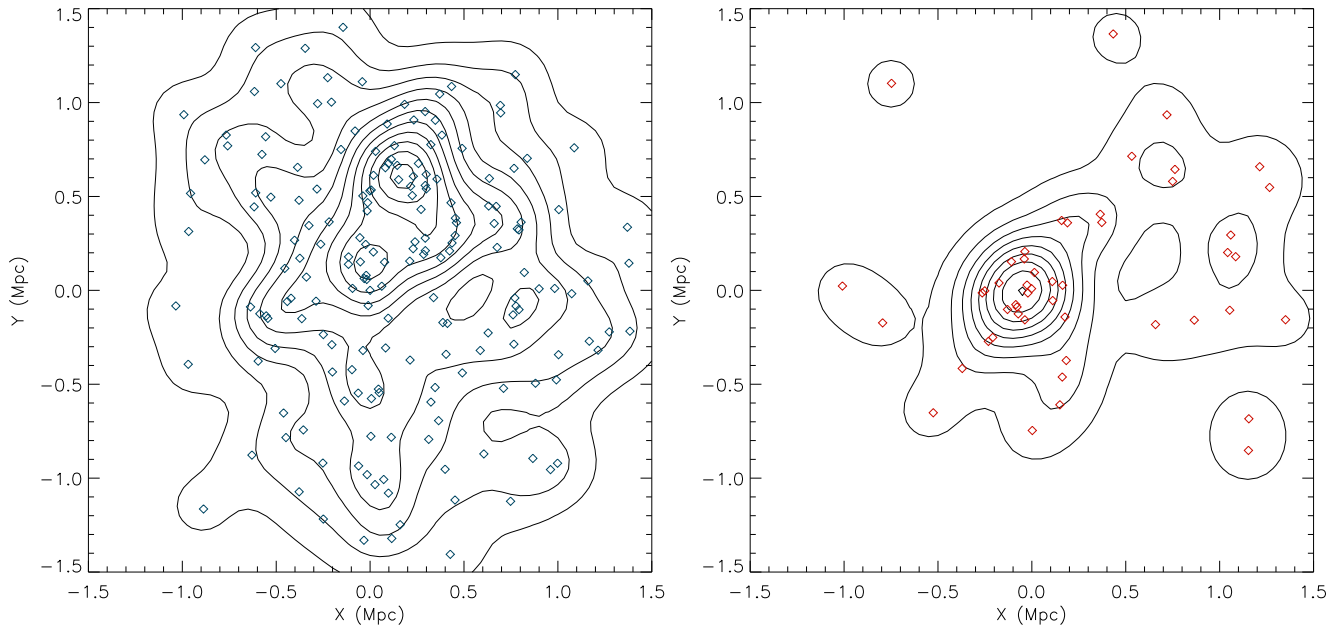


Figure 13. Spatial distribution of the two KMM velocity partitions. The positions of the galaxies are marked by open diamonds which are color coded according to the KMM partition they were allocated to (Figure 11). The contours show the adaptively smoothed galaxy surface density levels, beginning at 5 galaxies/Mpc and increasing by 10 gals/Mpc.

Radial gradients in the cluster velocity dispersion are expected and, in particular, the velocity dispersion is expected to decrease at larger radii due to a combination of the radial orbits of infalling galaxies and the decreasing escape velocity of the cluster. This can cause spurious results in 3D tests, such as the κ -test used here, which are not related to dynamical substructures (Pinkney et al. 1996). For this reason, we re-ran the κ -test considering only those galaxies residing within a central 1.5 Mpc radius region. Again, we find the observed value of $\kappa = 200$ does not occur in any of the 10,000 Monte Carlo realizations and lies $\sim 3.6\sigma$ from the mean of the simulated κ distribution, which has $\mu(\ln \kappa) = 4.58$ and $\sigma(\ln \kappa) = 0.20$.

The κ -test is an excellent tool for locating dynamically distinct substructure, however it provides no insight into the origin of the differences in the kinematics of the galaxies within the substructures. As a first step towards visualizing and characterizing the substructure revealed by the κ -test in Figure 14, we present Figure 15 which shows the line-of-sight velocity field. The value of each pixel in the line-of-sight velocity field map is the trimmed mean of the velocity distribution for the 15 nearest neighbors in projection. Only pixels where the radius to the 15th nearest neighbor is ≤ 1000 kpc are presented in Figure 15. The trimmed mean is measured by first determining the median and median absolute deviation (which are insensitive to outliers) as proxies for the mean and standard deviation for the distribution, trimming those points which are further than 3σ from the median and calculating the mean of the remaining points. The velocity field is complex and, most significantly, there is clear evidence for velocity structure within the central 1 Mpc region where a low velocity (~ -1300 km s $^{-1}$) structure is seen to the north, while a high velocity structure (~ 2400 km s $^{-1}$) is seen to the south. These two structures coincide with the two substructures revealed by the κ -test in Figure 14.

We now attempt to disentangle these substructures and ascertain their dynamics. To do this, we again utilize the KMM algorithm of Ashman et al. (1994) as in Section 4.1, however, here we use both spatial and velocity information to partition the cluster into its dynamical substructures. Since we are mainly interested in the dynamics of the central region, where we have *Chandra* data, and the KMM algorithm can be biased by outliers, we consider only members within a cluster-centric radius of 1.5 Mpc for the KMM analysis. As input, the KMM algorithm requires the number of partitions needed to describe the data, as well as the approximate mixing proportions and estimates of the means and covariance matrices for each partition. One of the major uncertainties when using this method is in determining the number of partitions required to adequately describe the data. We implement two strategies to overcome this uncertainty. First, we use the results from the κ -test, in combination with the galaxy surface density maps, to guide us in selecting the number of likely substructures. Second, we utilize the hypothesis testing capabilities of the KMM algorithm by measuring the LRTS, which gives a measure of the improvement in the fit for a complex, g -partition, model over a simpler, g_0 -partition model. In Ashman et al. (1994), the simpler model was a unimodal one (i.e., $g_0 = 1$) where the significance of the LRTS, expressed as a P -value, was estimated by comparison with a χ^2 distribution, which is only suitable when comparing two homoscedastic (i.e., the same variance), univariate models—clearly not the case here. Furthermore, we would like to assess how significantly the fit is improved by the addition of one partition, i.e., the g -partition case over the $g_0 = g - 1$ -partition case, in order to decide how many partitions to use. Therefore, we employ a parametric bootstrap resampling technique to determine the P -values as follows. We use KMM to fit the g_0 - and g -partition 3D Gaussian models to the data. We then produce 5000 bootstrapped samples by randomly sampling

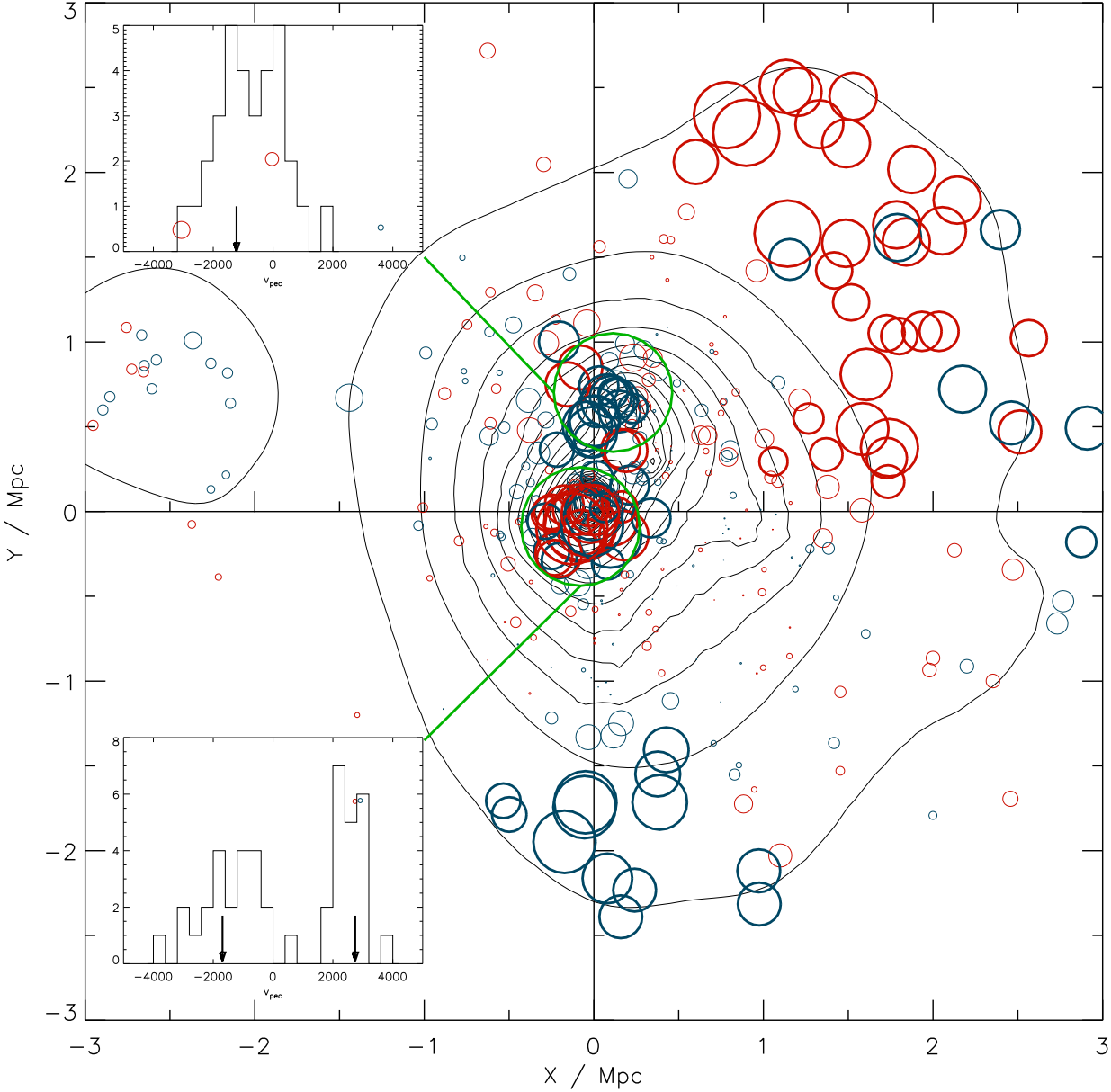


Figure 14. Bubble plot outputs from the κ test. The *bold* bubbles are those deemed to be significant inasmuch as they only occur in 1% of 10,000 realizations. The total κ test is significant at the 6.6σ level and the observed value does not occur in all 10,000 realizations. *Blue* and *red* bubbles have negative and positive v_{pec} , respectively. The contours are galaxy density contours generated from the adaptively smoothed image in the top left panel of Figure 12 and are linearly spaced by 10 in the interval 5-245 gals Mpc^{-2} . Note the two clusterings of significant bubbles are coincident with overdensities in the projected galaxy density. The inset panels show the peculiar velocity histograms for the regions indicated by the green circles, which have radii of 350 kpc. The arrows mark the velocities of the bright ($r_F < 17.8$) member galaxies within each green region.

the best fitting g_0 -partition 3D Gaussian mixture model. To each of these bootstrap samples, we re-fit the g_0 - and g -partition models, using the means and covariances of the models fitted to the data as initial input estimates for the KMM algorithm and remeasure the LRTS. The observed value for the LRTS is then compared to the null distribution of bootstrapped LRTS values to determine the P -value.

Figure 14 reveals two clear substructures: one with $v_{pec} \sim 2300 \text{ km s}^{-1}$ close to the cluster center, which we label Clump A and one with $v_{pec} \sim -1600 \text{ km s}^{-1}$ and

$\sim 700 \text{ kpc}$ north of the cluster center, which we label Clump B. There is also a possible substructure approximately spatially coincident with Clump A, but with a v_{pec} similar to that of Clump B, which we call Clump C. These partitions were used as input for the KMM algorithm. Thus, we fit three models: a $g = 2$ -, $g = 3$ - and $g = 4$ -partition model and at each stage we determine the P -value for the null hypothesis $g_0 = g - 1$ fit, as outlined above. To determine the initial estimates for input into the KMM algorithm, we take advantage of the fact that each of these clumps houses a

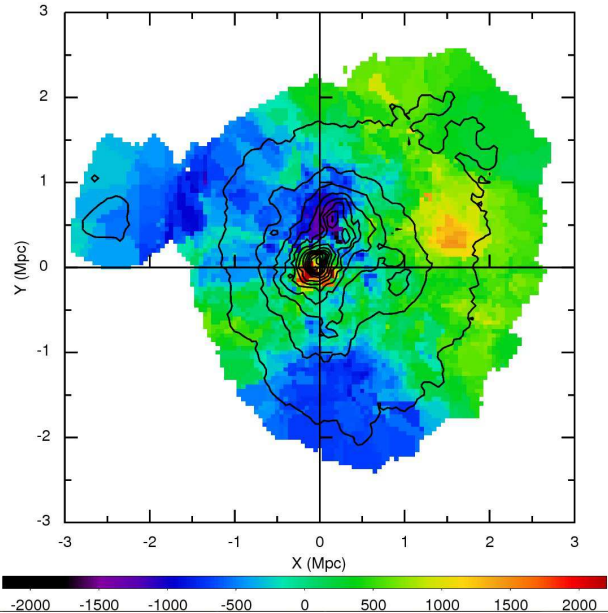


Figure 15. The line-of-sight velocity field determined at each pixel using the trimmed mean of the velocity distribution of the 15 nearest galaxies. The black contours show the galaxy density isopleths and the pixel size is 50 kpc.

bright ($r_F < 17.8$) galaxy which has v_{pec} at the peak of the velocity distribution (Figure 14). We assume that these bright galaxies lie at the spatial and dynamical centers of each partition and crudely define partition membership as any galaxy within $v_{pec} = \pm 1500 \text{ km s}^{-1}$ and radius $\leq 350 \text{ kpc}$ of the central galaxy. The means and covariance arrays for these initial partitions serve as the initial estimates for the KMM algorithm. The results of the $g = 2, 3$ and 4-partition KMM fits are presented in Figure 16. The P -values for these fits are $P_{g=2} < 0.0002$, $P_{g=3} = 0.02$, and $P_{g=4} = 0.93$. Thus, the $g = 3$ partition fit, with Clumps B and C combined, is the statistically preferred one, despite a spatial separation of $\sim 700 \text{ kpc}$ between the two bright galaxies in these clumps.

5. THE NATURE OF THE DETECTED SUBSTRUCTURES.

In this section, we discuss the relationship between the structures detected in the X-ray and optical analyses and present interpretations of the nature of these structures. As a visual aid to the discussion below, we present Figure 17 which is an R -band image taken with the AAT. Overlaid are contours from the X-ray residual map (Figure 2) showing the relevant X-ray substructures. The cluster member positions are overplotted and color coded to match the allocations from the KMM $g = 4$ partition (Section 4.3). While this partition was not found to be favored over a $g = 3$ partition fit, it serves the purpose of a visual aid by highlighting the dynamical structures discussed below in a more coherent manner.

5.1. The Northern core and northern major remnant core

In their analysis of the dynamics of Abell 2744, Boschin et al. (2006) detect the northern major remnant core in both the 2D and 3D analyses but discard the hypothesis that it is the undisturbed remnant core of the

main cluster. The combination of the new *Chandra* X-ray data and comprehensive AAOmega spectroscopy reveal that the substructure north of the central regions of Abell 2744 is more significant than previously thought. The strongest evidence for this assertion comes from Figure 13 which shows that when the contribution to the galaxy surface density from the high velocity southern component is removed, the most significant peak in the galaxy surface density is coincident with the northern substructure. In Section 4.3, we show that this galaxy surface density enhancement is detected as a dynamically distinct substructure with $v_{pec} \sim -1600 \text{ km s}^{-1}$ and $\sigma_v \sim 800 \text{ km s}^{-1}$. Furthermore, the deeper *Chandra* observations resolve a gas substructure and reveal a tail of gas trailing to the south which curves towards the west (Figure 1). The abundance map presented in Section 2.3 (Figure 4) shows that this gas substructure has significantly higher metallicity than the global cluster value, while the analysis of detailed spectra (NC1 in Table 2) show that this gas structure has a significantly lower temperature ($kT \sim 7 \text{ keV}$) than the global cluster temperature.

Observations of relaxed clusters show that the central core regions are characterized by a steep decline in gas temperature and a corresponding increase in metallicity (Vikhlinin et al. 2005). Given these observations and the thermodynamic properties outlined above, we interpret the northern gas substructure as the remnant of a cool-core which has survived the merging activity. In addition to this, the large velocity dispersion, the significant number of galaxies in this region, along with the fact that this structure harbors one of the bright cluster members (with $v_{pec} \sim -1200 \text{ km s}^{-1}$), we postulate that this northern component has a significant mass and is the core of the more massive system involved in the central merger in Abell 2744.

5.2. The central tidal debris

This structure, located coincident in projection with the high velocity southern substructure (Section 5.3), but separated in peculiar velocity by $\sim 4000 \text{ km s}^{-1}$ as discussed in Section 4.3 (Figure 14 inset), has previously been interpreted as being the core of the main negative v_{pec} component in the Abell 2744 system (Kempner & David 2004; Boschin et al. 2006). This interpretation is supported by the local peak in the surface density of the galaxies and the presence of a luminous galaxy with $v_{pec} \sim -1600 \text{ km s}^{-1}$. However, as discussed in Section 4.2 (see also Figure 13), the peak in the projected galaxy density here is artificially enhanced by the high velocity southern substructure. When this is accounted for, it can be seen that the more significant peak in the galaxy surface density of the negative v_{pec} component is in fact the northern substructure, which we interpret as the remnant core of the main cluster, as discussed in Section 5.1.

Despite not being the core of the negative v_{pec} component, this structure is a dynamically distinct component with a $v_{pec} \sim -1600 \text{ km s}^{-1}$. In Section 4.3, we found that adding a component representing this structure to the KMM analysis failed to improve the fit significantly over the simpler 3-partition fit. Therefore, we tentatively identify this structure as tidal debris stripped from the

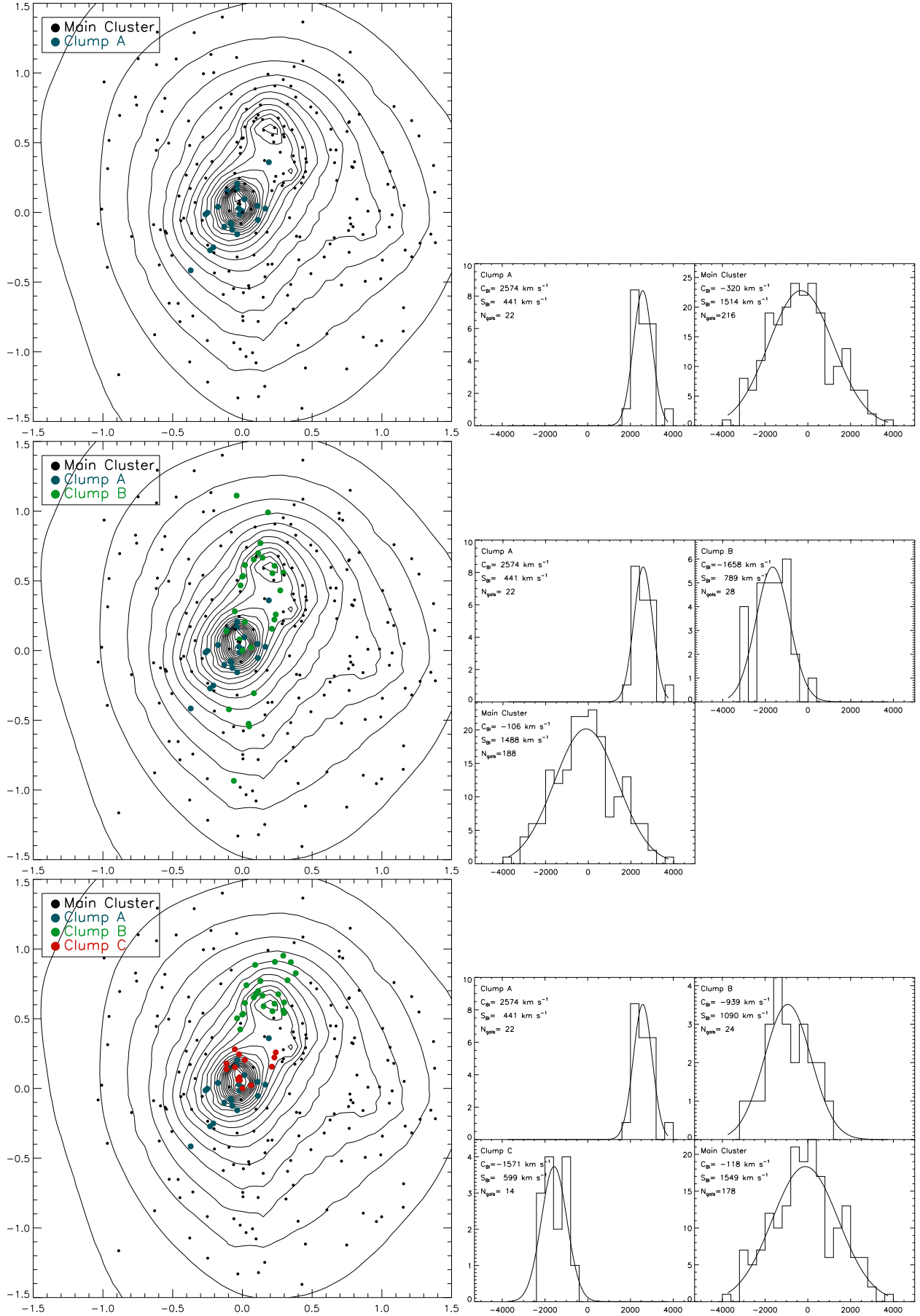


Figure 16. These plots show the results of the KMM partitioning of the data using the full spatial plus velocity information.

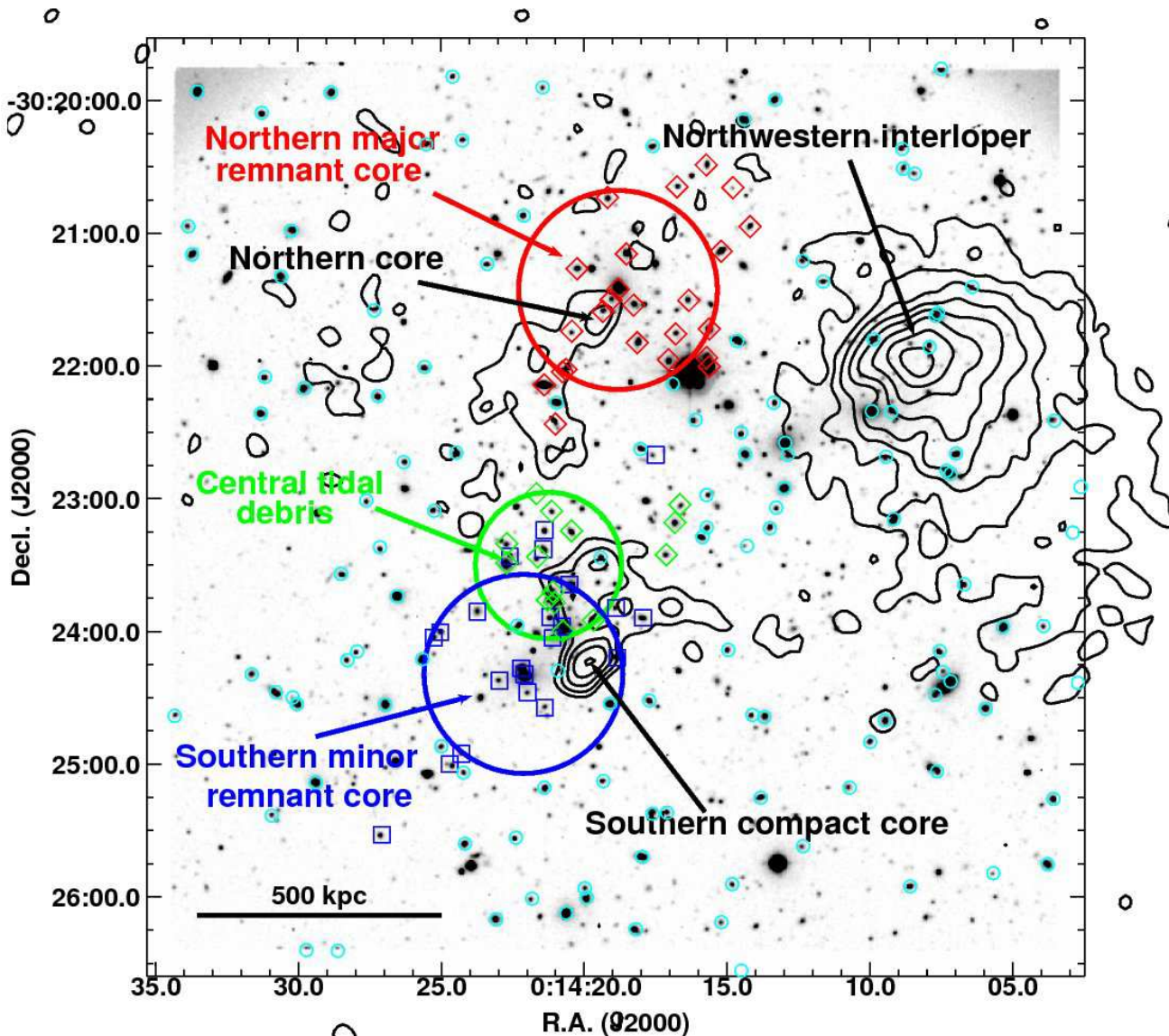


Figure 17. This image shows an AAT R -band image of Abell 2744. Contours from the X-ray residual map (Figure 2) are shown in black. The regions show cluster members and are color/shape coded with red diamonds, green diamonds, blue squares and cyan circles corresponding to members allocated to KMM partitions labeled in the lower left panel of Figure 16 as Clump B (Northern major remnant core), Clump C (Central tidal debris), Clump A (Southern minor remnant core) and the Main Cluster.

main cluster (the remnant core of which now lies mainly to the north) during the core passage phase of the merger with the high velocity southern substructure.

5.3. *The Southern compact core and southern minor remnant core: A Bullet-like remnant viewed from nearer to the merger axis*

The southern compact core stands out as a prominent surface brightness enhancement in the *Chandra* images (Figures 1 and 2). It is conspicuous in the thermodynamic maps presented in Section 2.3 as a region with significantly cooler, higher metallicity and lower entropy gas (Figures 3 and 4). This provides strong evidence for the southern compact core being the remnant cool core of a merging substructure. In Section 4.1 we found that the cluster peculiar velocity distribution was bimodal, containing a high velocity component. In Section 4.2 we explored the spatial distribution of this high velocity component, finding that it is spatially compact, while the combination of spatial and velocity information in Section 4.3 confirmed the existence of this structure as a dynamically distinct, spatially compact entity which we label as the southern minor remnant core in Figure 17. The proximity of the southern minor remnant core to the southern compact core indicates that they are associated; the bright galaxy accompanying the southern minor remnant core is located only ~ 140 kpc to the southeast of the X-ray peak due to the southern compact core. The peculiar velocity of the southern minor remnant core, obtained with the KMM analyses in Sections 4.1 (for the 1D velocity analysis) and 4.3 (for a full 3D velocity plus spatial information analysis), is $v_{pec} = 2300 - 2500$ km/s. We find evidence that the southern compact core also has a high peculiar velocity by considering the shock front to the southeast (Section 2.4.2). The Rankine-Hugoniot shock jump conditions can be used to derive a Mach number for the shock from the density jump and thus a shock velocity (e.g., Eqn 14 from Markevitch & Vikhlinin 2007; Landau & Lifshitz 1959). For the measured density jump of $1.60^{+0.17}_{-0.11}$, we determine a Mach number of $M = 1.41^{+0.113}_{-0.08}$. We can check this result by using Eqns 4 and 14 from Markevitch & Vikhlinin (2007) and the temperature measurements taken on either side of the front to obtain $M = 1.81^{+0.49}_{-0.37}$, consistent within the errors. The sound speed for a ~ 8.6 keV gas is ~ 1523 km/s, therefore the shock velocity is ~ 2150 km/s, using the Mach number derived from the density jump.

We note that this method does not give the total velocity of the shock, rather it gives the shock velocity in the plane of the sky. This is due to the following. In order that the shock front be observable as an edge in the surface brightness, our line of sight must be tangent to some point on the shock front surface. Assuming we know the radius of curvature, we measure the density jump at the point which is tangent to our line of sight. The Rankine-Hugoniot shock jump conditions relate the measured density jump to the Mach number of the component of gas velocity travelling perpendicular to the shock surface. Since our line of sight is tangent to the point at which we measure this Mach number, the measured velocity component must be in the plane of the sky. We can use this fact, in combination with the line of sight velocities of the northern major rem-

nant core and the southern minor remnant core, to constrain the inclination of the merger axis along the line of sight and to approximate the shock velocity. To do this, we assume that the southern compact and northern cores have the same line of sight velocities as their respective galaxy components, i.e., the southern minor and northern major remnant cores (measured from the 3D KMM partition in Section 4.3). The shock leading the southern compact core is meeting the unshocked gas associated with the northern core with a line of sight velocity $v_{los} \simeq 2574 + 1658 = 4232$ km s $^{-1}$ which, assuming the unshocked gas has $kT \sim 8.6$ keV, gives a line of sight Mach number of $M_{los} \simeq 4232/1523 = 2.78$. The inclination angle of the velocity vector to our line of sight is then $\arctan(1.41/2.78) \simeq 27^\circ$ and the total Mach number is $M_{tot} = 3.1$ leading to a shock speed of ~ 4750 km s $^{-1}$, similar to that observed in the Bullet cluster (Markevitch et al. 2002; Markevitch 2006). Using the Mach number derived from the temperature jump gives a similar value for the inclination angle of $\sim 33^\circ$, the total Mach number, $M_{tot} = 3.31$ and a shock speed of 5041 km s $^{-1}$. We note that, as in the Bullet cluster (Springel & Farrar 2007; Mastroiello & Burkert 2008), the shock velocity is measured relative to the surrounding gas which will have high bulk motions due to the merger. These measurements also rely critically on the assumption that the velocities of the gaseous and galactic components is the same. Future X-ray telescopes, such as the International X-ray Observatory, will have high enough spectral resolution to directly probe the line of sight gas kinematics and will enable us to test this assumption.

The measured velocity dispersion of the southern minor remnant core ranges from 581 km/s, measured from the 1D KMM partition, to 441 km/s, measured from the 3D KMM partition. This dispersion is likely to be an underestimate of the real dispersion due to the KMM partitioning which allocates objects which are probably physically associated with the southern minor remnant core, but in the tails of the velocity distribution, to the main cluster. This effect is seen in the right-most panel of Figure 11, which shows that objects with peculiar velocities overlapping with the main structure have been allocated to the main structure, thereby truncating the southern minor remnant core's velocity distribution. The act of merging will also affect the measured velocity dispersion, since the merger acts to disperse the southern minor remnant core's galaxies (Pinkney et al. 1996). The galaxies most likely to be stripped are those that are least tightly bound to the southern minor remnant core, e.g., those in the outskirts, or those in the tails of the velocity distribution. This stripping, compounded by the lack of certainty in the allocation of galaxies as members of the southern minor remnant core, mean it is extremely difficult to gauge the southern minor remnant core's initial velocity dispersion. In any case, the measured velocity dispersion indicates the southern minor remnant core contains significant mass, as does the measured temperature of ~ 7 keV for the southern compact core.

Given the above evidence, we interpret the southern compact core as a Bullet-like system (Markevitch et al. 2002) merging along an axis that lies well out of the plane of the sky. To support this interpretation, we present Figure 18, which shows a model for the X-ray appear-

ance of the Bullet cluster (as used in Bradač et al. 2006) viewed from a range of directions. Briefly, the *Chandra* X-ray image of the Bullet cluster is fitted with a density model which consists of a shuttlecock with concave sides (for the Bullet substructure), power-law profiles across the cold and shock fronts, a flattened pancake (for the main cluster’s emission) and a beta-model at larger radii. The XIM software (Heinz & Brüggen 2009) is used in combination with this density model to simulate 0.6–5 keV *Chandra* images with 100 ks exposures and projected so that the merger axis is inclined to our line of sight with angles of $\theta_{inc} = 90, 15, 35, 48, \text{ and } 60$. To best match the orientation of the southern compact core in Abell 2744, the images shown in the lower 4 panels of Figure 18 are again rotated in the plane of the sky.

Comparing the simulated images in Figure 18 with the X-ray morphology of the southern compact core, we surmise that an inclination angle in the range $\theta_{inc} = 35\text{--}60^\circ$ provides the best qualitative fit. This is based primarily on the observability of the shock front (Section 2.4.2) and on the blunted cone appearance of the southern compact core in the *Chandra* images (Figure 1). These inclination angles compare well with that derived above from the combination of the shock and kinematic parameters, particularly when considering uncertainties inherent in both techniques.

5.4. The northwestern interloper

In their analysis of the northwestern interloper, KD04 presented tentative evidence for a cold front and a bow shock on the eastern side of the northwestern interloper (their Figure 3.). In our deeper observations, we find no convincing evidence for the existence of a shock front at the position and orientation indicated in KD04. However, both of the putative fronts appear to be part of a larger front on the northeastern side of the northwestern interloper, as indicated in Figure 1. The analysis in Section 2.4.3 reveals that this is a cold front. In Figure 2 we noted that the emission surrounding the northwestern interloper extends towards the south. The analyses conducted in Sections 2.3 and 2.4 indicate that this extension is cooler and has lower entropy than the ICM immediately to the east and west. We interpret the low entropy gas as a trail of gas stripped from the northwestern interloper by ram pressure.

While we detect no dynamical system associated with the northwestern interloper, the pair of bright galaxies lying ~ 140 kpc and ~ 320 kpc southeast of the X-ray peak have peculiar velocities of 561 km s^{-1} and 663 km s^{-1} , respectively. The velocity field (Figure 15) has values of $\sim 400 \text{ km s}^{-1}$ in the region of the northwestern interloper, consistent with the velocities of the pair of bright galaxies. This hints at a dynamically distinct system. However, because the velocities are close to those of the main cluster and because of the small number of spectroscopically confirmed cluster members in this region, dynamical substructure is more difficult to detect at a significant level (Pinkney et al. 1996). We note also that if the northwestern interloper has passed pericenter, as we argue in Section 6.2, it is plausible that a large fraction of the galaxies have been tidally stripped. This will further inhibit the detection of dynamical substructure associated with the northwestern interloper.

Using the photometric redshift catalog of Busarello

et al. (2002) to define cluster members, probing ~ 1.3 mag fainter than our spectroscopy, we do detect a local peak in the galaxy surface density coincident with the northwestern interloper’s X-ray peak. We showed that the non-detection of a local peak in the 2D galaxy distribution of the spectroscopically confirmed cluster members is not due to spectroscopic incompleteness, but due to the majority of galaxies associated with the overdensity detected using the photometrically defined members having magnitudes fainter than our limiting magnitude for the spectroscopy. Thus, spectroscopic observations probing to fainter magnitudes are required to confirm the existence of a substructure associated with the northwestern interloper.

6. A MERGER SCENARIO

Here we present a merger scenario based on our new observations. Our interpretation of the data reveal a merger scenario which agrees with previous authors in the broadest sense, i.e., we are observing a major merger in the central regions of the cluster and a more minor infall of a group to the northwest. However, the details of our merger scenario differ from those outlined previously in KD04 and Boschin et al. (2006). In the following, we sketch an outline for this major-plus-minor-merger scenario, but stress that confirmation of our hypotheses require rigorous testing in the form of planned Abell 2744 specific merger simulations.

6.1. The central major merger

The central region of the cluster has extremely complex X-ray morphology, temperature and metallicity structure, as well as multiple dynamically distinct components. These features can be reconciled with an off center, two body merger after core passage, with the merger axis nearer to our line of sight than the plane of the sky. Below, we provide evidence for these assertions.

During cluster mergers, the strong ram pressure felt by the gas means that it can become decoupled from the collisionless galaxies which will lead the gas (e.g., Barrena et al. 2002; Markevitch et al. 2002; Clowe et al. 2006; Mahdavi et al. 2007; Bradač et al. 2008). From the observed offset between the galaxies and gas, the X-ray morphologies, and also the velocities of the subclusters, we can determine the direction of motion of the two subclusters. The northern major remnant core is blueshifted with respect to the systemic velocity of the cluster complex ($v_{pec} \simeq -1600 \text{ km s}^{-1}$), the galaxy substructure is offset from the northern core to the northwest, with the bright cluster galaxy associated with the remnant core leading by ~ 100 kpc. This evidence indicates that some component of the northern subcluster’s motion is directed towards the north-northwest, while a large portion is also directed towards us along the line of sight. Further evidence for the north-northwest motion is revealed by the enhanced X-ray emission to the southeast of the northern core (Figures 1 and 17), which we interpret as a trail of stripped gas. The curvature of the gas trail implies significant westward acceleration, so that the northward moving core must have passed to the east of the core of the other major subcluster, which we associate with the southern compact core.

Using a similar argument, we can ascertain the direction of motion of the southern subcluster. The brightest

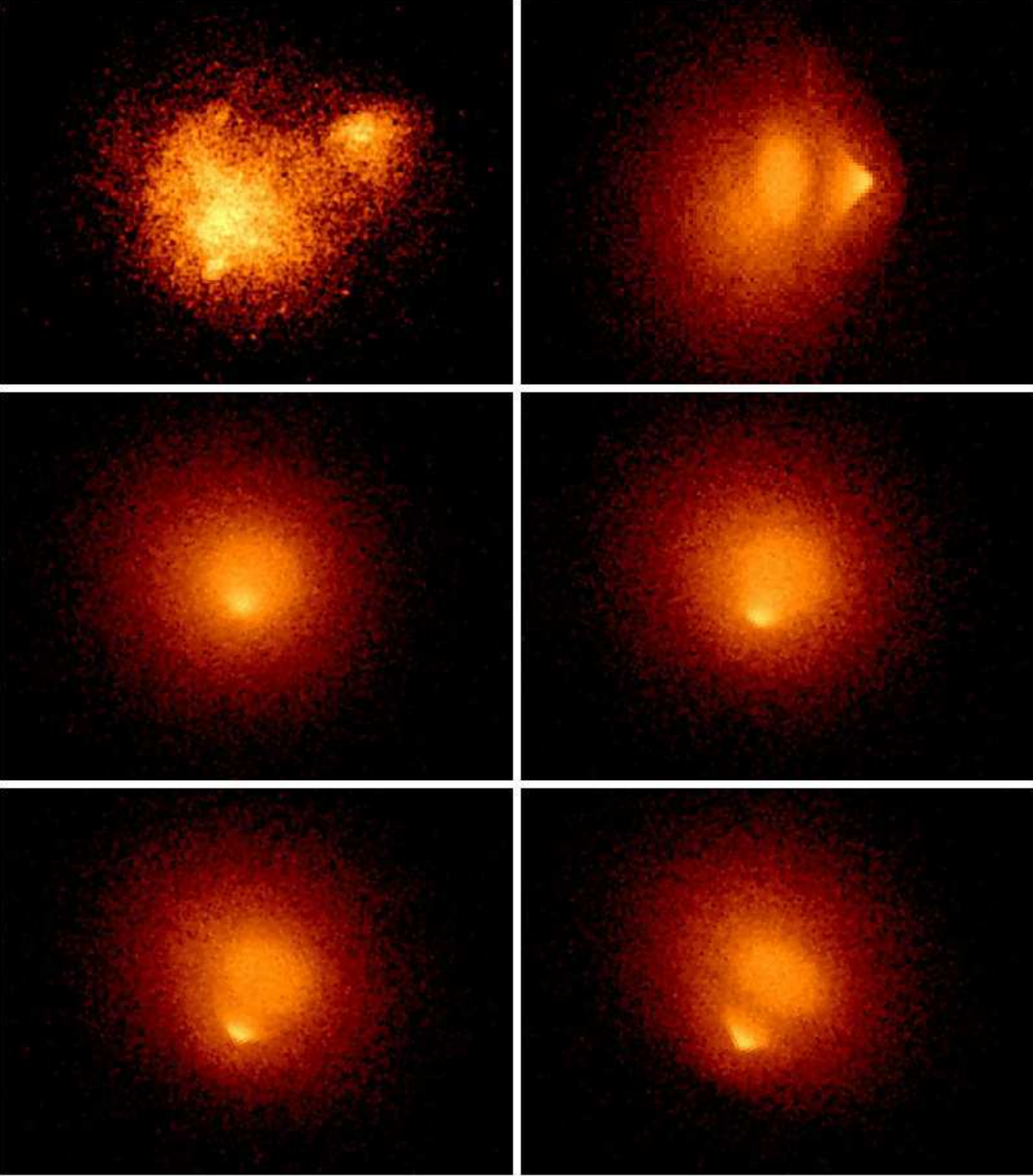


Figure 18. *Top left:* A2744 *Chandra* image. *Top Right:* Simulated 100ks *Chandra* ACIS-I observation of the Bullet cluster gas model (at $z=0.308$) viewed in the same projection as the Bullet cluster, i.e., $\theta_{inc} = 90$ where θ_{inc} gives the angle of the merger axis with respect to the line of sight. *Middle left:* As for *top right* with $\theta_{inc} = 15$. *Middle Right:* As for *top right* with $\theta_{inc} = 35$. *Bottom Left:* As for *top right* with $\theta_{inc} = 48$. *Bottom Right:* As for *top right* with $\theta_{inc} = 60$. The bottom four panels are rotated in the plane of the sky to best match the orientation of Abell 2744 shown in the top left panel.

galaxy associated with the southern minor remnant core is offset some ~ 140 kpc south of due east of the peak in the X-ray emission associated with the southern compact core and assuming that this bright galaxy was once at the center of the subcluster and coincident with the peak in the X-ray emission, this offset indicates some fraction of the southern subcluster's motion is directed towards the south-east. Further evidence for motion towards the southeast comes from the *Chandra* image in

the form of the edge to the southeast (Figure 1), which is part of the shock front (Section 5.3), and the morphology of the southern compact core, which exhibits a blunted cone structure where the compact core is the head of the blunted cone, and the tail of stripped gas to the northwest forms a wedge-like structure. The mean peculiar velocity of the southern minor remnant core galaxies ($\sim 2300 - 2500 \text{ km s}^{-1}$) indicates that a large fraction of the southern substructure's motion is directed away from

us along our line of sight. However, the edge and blunted cone morphology of the southern compact core show that the direction of motion cannot be entirely directed along our line-of-sight.

These arguments require that the northern and southern subclusters have passed one another and now are moving apart. The gaseous envelopes of the two subclusters have largely been stopped and stripped from their former hosts by shocks, separating them from the remnant cool cores, which can survive the off-center merger due to their higher densities and pressures. In our merger scenario, the central peak of emission is the gas which has been stripped from the outer parts of the two subclusters during the core passage phase of the merger. This interpretation is supported by high temperatures in the central gas, consistent with shock heating and adiabatic compression during the core passage. Patches of low metallicity gas suggest that at least some of this gas originates from outside the more highly enriched cores (Vikhlinin et al. 2005), as described above.

According to the KMM partitioning in Section 4.3, a majority (188 out of 238) of the galaxies are allocated to a partition with $\mu = -105 \text{ km s}^{-1}$ and $\sigma = 1438 \text{ km s}^{-1}$. This is also clearly seen in Figure 10 where within a cluster-centric radius of 500 kpc there is a clear segregation in velocity with essentially no galaxies with $v_{pec} = 0 \text{ km s}^{-1}$, whereas at $R > 500 \text{ kpc}$ the velocity distribution appears to be unimodal and centered around $v_{pec} = 0 \text{ km s}^{-1}$. Presumably the galaxies at larger radii were once part of the less-tightly-bound outskirts of the southern and northern substructures. The outskirts of the two merging clusters decoupled from the tightly bound cores during pericenter and are in the process of mixing to form the outskirts of the new cluster.

In our interpretation, the northern subcluster was the more massive of the two merging systems and the southern subcluster is the remnant of the less massive one, consistent with the higher velocity dispersion of the northern major remnant core. However, the southern compact core is brighter now. This suggests that the smaller subcluster hosted a more robust cool core, i.e. a greater mass of low entropy gas, prior to the merger. The higher entropy northern core of the larger subcluster would then be more prone to disruption during the merger. Indeed, the clumpy tail of gas trailing the northern core indicates that a significant fraction of its gas has been removed and it is in the process of being destroyed by the merger.

6.2. *The infall of the northwestern interloper*

The deeper Chandra observations presented here fail to confirm the proposal by KD04 that the northwestern interloper is traveling eastward on its first passage through the cluster. KD04 used the positions of two bright cluster galaxies $\sim 140 \text{ kpc}$ and $\sim 320 \text{ kpc}$ southeast of the northwestern interloper, along with tentative detections of cold and shock fronts on the eastern side of the interloper, to support this scenario. We find little evidence for the shock proposed to exist by KD04, while their proposed cold front is part of a more extended cold front. Furthermore, it is difficult to explain the large separation of gas and galaxies prior to a core passage in a subcluster which appears to have both significant mass (indicated by its temperature $kT \sim 5 \text{ keV}$) and ICM density (indicated by its X-ray brightness).

Three main features in the deeper X-ray data provide support for an alternative interpretation. They are 1) the cold front to the north-east, 2) the extended region of enhanced X-ray surface brightness to the south and 3) the swirl of low entropy gas seen in Figure 3, which is associated with the southern extension and is curved in a southeasterly direction towards the cluster center. The cold front to the north-east, along with the extension of the emission towards the south, indicate that the northwestern interloper is currently traveling towards the north-northeast. The curvature of the swirl of low entropy gas indicates significant angular momentum. Using these features to guide our interpretation, we suggest that the northwestern interloper fell into the main cluster from the south or southeast, initially traveling roughly north or northwest and passing the main cluster core off-center to the southwest. The gravity of the main cluster has subsequently deflected it onto its current path towards the north-northeast (see, e.g., the evolution of the 3:1 and 10:1 mass ratio, offcenter mergers in Poole et al. 2006). The fact these features are observed at all, along with the non-detection of any significant dynamical substructure in this region, indicates the merger of the northwestern interloper is taking place fairly close to the plane of the sky. We note, however, that the non-detection of dynamical activity here may be due to the limited depth and completeness of our sample.

One issue with the above interpretation for the northwestern interloper is the position of the two bright galaxies which are offset to the southeast from the peak in the X-ray emission. Assuming these bright galaxies trace the dominant mass component (i.e., the collisionless dark matter core) of the northwestern subcluster, we would expect to see the classic Bullet-like scenario where the collisionless dark matter and galaxies lead the collisional gas component and thus to see the bright galaxies offset to the northeast of the gas clump. However, we note that during the later stages of a merger, the simulations of Mathis et al. (2005) showed that the cool, dense cores of subclusters can lead the dark matter cores. Indeed, this phenomenon has been observed in the clusters Abell 168 (Hallman & Markevitch 2004) and Abell 754 (Markevitch et al. 2003). The physical mechanism producing this offset is the rapid changes in ram pressure felt by the subcluster gas as it traverses the main cluster; during closest approach, the ram pressure peaks and the gas and dark matter separate, with the dark matter leading. After the core passage phase, the ram pressure drops significantly due to the decrease in the surrounding ICM density and the cool core begins to fall back towards its parent dark matter core, eventually overshooting it in a “ram pressure slingshot” as explained in Markevitch & Vikhlinin (2007). This effect is also simulated in Ascasibar & Markevitch (2006) and their Figure 12 shows qualitative agreement with what is proposed above and with the temperature morphology of the northwestern substructure. High resolution weak lensing maps are required to determine the location of the local peak in the mass density corresponding to the northwestern interloper and to test the scenario outlined above.

While the northwestern subcluster is due to a more minor merger than the central merger, there should still be observable effects due to the core passage, particularly in the ICM. Although the central major merger complicates

this matter and may erase any effects due to the north-western subcluster, we tentatively point out the bridge of emission in Figure 1 along with the slight asymmetry of the central cluster emission in the direction of the north-western interloper, as evidence of the previous interaction with the central ICM. We also suggest that the hot regions lying between the main cluster and the north-western interloper (Figure 3) were produced by shocks and/or compression of the ICM during the subclusters passage.

6.3. Comparison to previous interpretations

The interpretations outlined above for the different structures revealed by our new observations give cause to re-visit the hypotheses outlined in Boschin et al. (2006) and KD04 for the merging history of Abell 2744. Considering the central regions, KD04 propose a merger scenario where Abell 2744 is seen just prior to a core passage and the merger is occurring along a north-south direction with the majority of the motion directed along our line-of-sight. Boschin et al. (2006), using a slightly larger sample of spectroscopically confirmed cluster members, agreed with KD04 that the central merger is occurring along a north-south direction with the majority of the motion directed along our line-of-sight, but suggested that the merger is in a more advanced post-core-passage phase. Both KD04 and Boschin et al. (2006) suggest that the northwestern subcluster is infalling onto the main cluster from the west and can be treated as separate from the major merger occurring in the central regions.

With regard to the southern subcluster, our interpretation of the new observations is mostly in accordance with the conclusion of Boschin et al. (2006) that it is viewed after a core passage, has a large fraction of its motion directed along the line-of-sight and some component to the south. We slightly modify this scenario based on the detection of the shock front and the blunted cone X-ray morphology, which indicate a more southeasterly direction of motion. The detection of the shock front also indicates that the component of the velocity perpendicular to our line-of-sight must be larger than previously suggested. Indeed, our observations of the shock front, combined with the dynamical analyses, allow us to constrain the direction of motion of the southern subcluster to be inclined at around 30° to the line of sight.

Our scenario differs most from that of Boschin et al. (2006) in the importance of the northern subcluster. Boschin et al. (2006) interpret this structure as an additional feature in their scenario due to the lack of a counterpart in the X-ray images. Our deeper *Chandra* data reveals the northern core as a cool, high metallicity structure which is trailing the dynamically distinct northern major remnant core galaxies. Furthermore, the larger sample of spectroscopically confirmed cluster members provide strong evidence that, when separated by velocity, the most significant projected galaxy overdensity is the northern major remnant core. Taking these new results in concert provides strong evidence in support of our view that the northern subcluster is the surviving core of the main component involved in the central merger. Thus, while we agree with Boschin et al. (2006) that we are observing a post-core passage merger in the central regions, we suggest a somewhat later phase, given the large (~ 800 kpc) projected separation of the main

northern subcluster from the high velocity southern subcluster.

Turning to the interloping northwestern subcluster, the deeper *Chandra* data have muddied the waters somewhat in terms of a simple interpretation and indicate that the direction of motion of this subcluster is currently to the north/northeast—perpendicular to the direction of motion suggested by both KD04 and Boschin et al. (2006). Both Boschin et al. (2006) and Braglia et al. (2009) detect an overdensity of red galaxies associated with the bright cluster galaxy lying ~ 140 kpc to the southeast of the X-ray peak. We propose that this offset has occurred due to a ram pressure slingshot which caused the gas to “overshoot” the galaxies after pericentric passage. This interpretation provides a better fit to the X-ray data and we note that the galaxy overdensities found here and in the Boschin et al. (2006) and Braglia et al. (2009) studies rely on photometric cluster member allocation, rather than the more robust spectroscopic identification of cluster members, which is less prone to projection effects. A more rigorous investigation involving deeper spectroscopy and detailed simulations are required to test the different infall scenarios for this substructure.

7. SUMMARY AND CONCLUSIONS

We have presented an analysis of the merging cluster Abell 2744 based on new *Chandra* X-ray data and AAOmega optical spectroscopy. The deeper *Chandra* data reveal a plethora of substructure including:

1. A significant structure to the north with a trail of X-ray emission to the south and curving westward. This northern core harbors cooler gas with higher metallicity than its surroundings, indicating it is a remnant cool core.
2. The Bullet-like southern compact core which is surrounded by hot, shocked gas. There is an edge to the southeast of the southern compact core, which has the characteristics of a shock front with a Mach number $M = 1.41^{+0.13}_{-0.08}$.
3. A global peak in the X-ray emission with no corresponding galaxy overdensity, which is interpreted as the stripped atmospheres of the merging subclusters.
4. The northwestern interloper has an edge to the northeast and a tail of emission extending towards the south. Analysis of the spectra of these features indicate that the edge is a cold front and that the tail of gas harbors cooler, lower entropy gas when compared to the surrounding gas.

From the new AAOmega optical spectroscopy, we have found:

1. From 343 spectroscopically confirmed members within a 3 Mpc radius, the redshift and velocity dispersion of Abell 2744 are, respectively, $z_{clus} = 0.3064 \pm 0.0004$ and $\sigma = 1497 \pm 47$ km s $^{-1}$.
2. The velocity distribution is significantly skewed and the KMM analysis reveals the velocity distribution in the central region is characterized by two distinct structures in velocity space, separated by ~ 3000 km s $^{-1}$.

3. Examination of the spatial distribution of the galaxies within the two partitions found in the KMM analysis of the velocity distribution reveal that for the negative peculiar velocity component the more significant galaxy concentration lies further to the north, approximately coincident with the cool, high metallicity northern core revealed by the *Chandra* data.
4. Applying the KMM algorithm to the combined velocity and spatial information, we find the statistically favored fit is one where the sample is partitioned into three. Two of the partitions correspond to the remnant cores of the two merging clusters in the central regions, while the third likely contains the galaxies which were in the outskirts of the two subclusters and are currently in the process of mixing to form the new cluster. The third substructure also contains those galaxies which belong to the northwestern interloper.
5. The northwestern interloper detected in the *Chandra* image is not detected as a dynamical substructure, nor as a substructure in local galaxy surface density when considering only spectroscopically confirmed members. An increase in local galaxy surface density is detected when considering cluster members defined using photometric redshifts, although only when including galaxies down to magnitude $R=22.3$.

In combination, the observations presented here have been used to outline a skeleton hypothesis for the merger history of Abell 2744. In this scenario, we have identified two significant subclusters in the central region which have undergone a violent core passage and are now moving away from each other along a roughly north-south axis, with a large line-of-sight component. For the northwestern subcluster, we propose a scenario where the structure is traveling to the north/northeast after pericenter. Confirmation of this merger hypothesis requires detailed simulations and deeper optical spectroscopy in the central regions in order to probe the dynamics of the northwestern subcluster.

The evidence for a post-core passage merger phase reported here, along with the significant enhancement of blue starburst and poststarburst galaxies residing within Abell 2744 (Couch et al. 1998), provides further evidence that major cluster mergers can act as catalysts for rapid, environmentally driven evolution in the star forming properties of cluster galaxies and that this evolution occurs when the cluster galaxy environment is violently rearranged during the core passage phase of a major merger. Our large spectroscopic sample, in combination with deep radio data, can now be used to define a large sample of actively transforming galaxies which will further test this hypothesis of merger-induced galaxy transformation.

We thank Gregory Poole for useful discussions and sanity checks. We are grateful to Will Saunders and the staff at the Anglo-Australian Observatory for their support during AAT observations. We thank Lee Spitler for his assistance in preparing the AAT image and Emily Wisnioski for supplying code for the PCA sky subtraction.

We acknowledge the financial support of the Australian Research Council (via its Discovery Project Scheme) throughout the course of this work. PEJN was partly supported by NASA grant NAS8-03060. This work was partly supported through Chandra GO7-8127X. This research has made use of software provided by the Chandra X-ray Center (CXC) in the application packages CIAO, ChIPS, and Sherpa and also of data obtained from the Chandra archive at the NASA Chandra X-ray center (<http://cxc.harvard.edu/cda/>). This research has made use of the NASA/IPAC Extragalactic Database (NED) which is operated by the Jet Propulsion Laboratory, California Institute of Technology, under contract with the National Aeronautics and Space Administration.

Facilities: CXO (ACIS), AAT (AAOmega)

REFERENCES

- Abell, G. O., Corwin, Jr., H. G., & Olowin, R. P. 1989, *ApJS*, 70, 1
- Anders, E., & Grevesse, N. 1989, *Geochim. Cosmochim. Acta*, 53, 197
- Andreon, S. 2001, *ApJ*, 547, 623
- Arnaud, K. A. 1996, in *Astronomical Society of the Pacific Conference Series*, Vol. 101, *Astronomical Data Analysis Software and Systems V*, ed. G. H. Jacoby & J. Barnes, 17–+
- Ascasibar, Y., & Markevitch, M. 2006, *ApJ*, 650, 102
- Ashman, K. M., Bird, C. M., & Zepf, S. E. 1994, *AJ*, 108, 2348
- Barrena, R., Biviano, A., Ramella, M., Falco, E. E., & Seitz, S. 2002, *A&A*, 386, 816
- Barrena, R., Boschin, W., Girardi, M., & Spolaor, M. 2007, *A&A*, 467, 37
- Beers, T. C., Flynn, K., & Gebhardt, K. 1990, *AJ*, 100, 32
- Bekki, K., Owers, M. S., & Couch, W. J. 2010, *ApJ*, 718, L27
- Boschin, W., Girardi, M., Spolaor, M., & Barrena, R. 2006, *A&A*, 449, 461
- Bradač, M., Allen, S. W., Treu, T., Ebeling, H., Massey, R., Morris, R. G., von der Linden, A., & Applegate, D. 2008, *ArXiv e-prints*, 806
- Bradač, M., Clowe, D., Gonzalez, A. H., Marshall, P., Forman, W., Jones, C., Markevitch, M., Randall, S., Schrabback, T., & Zaritsky, D. 2006, *ApJ*, 652, 937
- Braglia, F., Pierini, D., & Böhringer, H. 2007, *A&A*, 470, 425
- Braglia, F. G., Pierini, D., Biviano, A., & Böhringer, H. 2009, *A&A*, 500, 947
- Burgett, W. S., Vick, M. M., Davis, D. S., Colless, M., De Propriis, R., Baldry, I., Baugh, C., Bland-Hawthorn, J., Bridges, T., Cannon, R., Cole, S., Collins, C., Couch, W., Cross, N., Dalton, G., Driver, S., Efstathiou, G., Ellis, R., Frenk, C. S., Glazebrook, K., Hawkins, E., Jackson, C., Lahav, O., Lewis, I., Lumsden, S., Maddox, S., Madgwick, D., Norberg, P., Peacock, J. A., Percival, W., Peterson, B., Sutherland, W., & Taylor, K. 2004, *MNRAS*, 352, 605
- Busarello, G., Merluzzi, P., La Barbera, F., Massarotti, M., & Capaccioli, M. 2002, *A&A*, 389, 787
- Butcher, H., & Oemler, Jr., A. 1978, *ApJ*, 219, 18
- . 1984, *ApJ*, 285, 426
- Caldwell, N., & Rose, J. A. 1997, *AJ*, 113, 492
- Caldwell, N., Rose, J. A., Sharples, R. M., Ellis, R. S., & Bower, R. G. 1993, *AJ*, 106, 473
- Cappellari, M., & Copin, Y. 2003, *MNRAS*, 342, 345
- Clowe, D., Bradač, M., Gonzalez, A. H., Markevitch, M., Randall, S. W., Jones, C., & Zaritsky, D. 2006, *ApJ*, 648, L109
- Colless, M., Dalton, G., Maddox, S., Sutherland, W., Norberg, P., Cole, S., Bland-Hawthorn, J., Bridges, T., Cannon, R., Collins, C., Couch, W., Cross, N., Deeley, K., De Propriis, R., Driver, S. P., Efstathiou, G., Ellis, R. S., Frenk, C. S., Glazebrook, K., Jackson, C., Lahav, O., Lewis, I., Lumsden, S., Madgwick, D., Peacock, J. A., Peterson, B. A., Price, I., Seaborne, M., & Taylor, K. 2001, *MNRAS*, 328, 1039
- Colless, M., & Dunn, A. M. 1996, *ApJ*, 458, 435
- Couch, W. J., Barger, A. J., Smail, I., Ellis, R. S., & Sharples, R. M. 1998, *ApJ*, 497, 188

- Couch, W. J., & Newell, E. B. 1984, *ApJS*, 56, 143
- Couch, W. J., & Sharples, R. M. 1987, *MNRAS*, 229, 423
- Desai, V., Dalcanton, J. J., Aragón-Salamanca, A., Jablonka, P., Poggianti, B., Gogarten, S. M., Simard, L., Milvang-Jensen, B., Rudnick, G., Zaritsky, D., Clowe, D., Halliday, C., Pelló, R., Saglia, R., & White, S. 2007, *ApJ*, 660, 1151
- Dickey, J. M., & Lockman, F. J. 1990, *ARA&A*, 28, 215
- Diehl, S., & Statler, T. S. 2006, *MNRAS*, 368, 497
- Dressler, A., Oemler, A. J., Couch, W. J., Smail, I., Ellis, R. S., Barger, A., Butcher, H., Poggianti, B. M., & Sharples, R. M. 1997, *ApJ*, 490, 577
- Dressler, A., & Shectman, S. A. 1988, *AJ*, 95, 985
- Drinkwater, M. J., Jurek, R. J., Blake, C., Woods, D., Pimblett, K. A., Glazebrook, K., Sharp, R., Pracy, M. B., Brough, S., Colless, M., Couch, W. J., Croom, S. M., Davis, T. M., Forbes, D., Forster, K., Gilbank, D. G., Gladders, M., Jelliffe, B., Jones, N., Li, I., Madore, B., Martin, D. C., Poole, G. B., Small, T., Wisnioski, E., Wyder, T., & Yee, H. K. C. 2010, *MNRAS*, 401, 1429
- Fadda, D., Girardi, M., Giuricin, G., Mardirossian, F., & Mezzetti, M. 1996, *ApJ*, 473, 670
- Fasano, G., Poggianti, B. M., Couch, W. J., Bettoni, D., Kjærgaard, P., & Moles, M. 2000, *ApJ*, 542, 673
- Finoguenov, A., Böhringer, H., & Zhang, Y. 2005, *A&A*, 442, 827
- Giovannini, G., Tordi, M., & Feretti, L. 1999, *New Astronomy*, 4, 141
- Girardi, M., & Mezzetti, M. 2001, *ApJ*, 548, 79
- Govoni, F., Enßlin, T. A., Feretti, L., & Giovannini, G. 2001a, *A&A*, 369, 441
- Govoni, F., Feretti, L., Giovannini, G., Böhringer, H., Reiprich, T. H., & Murgia, M. 2001b, *A&A*, 376, 803
- Hallman, E. J., & Markevitch, M. 2004, *ApJ*, 610, L81
- Hambly, N. C., Irwin, M. J., & MacGillivray, H. T. 2001, *MNRAS*, 326, 1295
- Heinz, S., & Brüggén, M. 2009, *ArXiv e-prints*
- Hwang, H. S., & Lee, M. G. 2009, *MNRAS*, 397, 2111
- Johnston-Hollitt, M., Sato, M., Gill, J. A., Fleenor, M. C., & Brick, A. 2008, *MNRAS*, 390, 289
- Just, D. W., Zaritsky, D., Sand, D. J., Desai, V., & Rudnick, G. 2010, *ApJ*, 711, 192
- Kaastra, J. S. 1992, *An X-Ray Spectral Code for Optically Thin Plasmas* (Internal SRON-Leiden Report, updated version 2.0)
- Kauffmann, G. 1995, *MNRAS*, 274, 153
- Kempner, J. C., & David, L. P. 2004, *MNRAS*, 349, 385
- Kurtz, M. J., & Mink, D. J. 1998, *PASP*, 110, 934
- Landau, L. D., & Lifshitz, E. M. 1959, *Fluid mechanics*, ed. Landau, L. D. & Lifshitz, E. M.
- Liedahl, D. A., Osterheld, A. L., & Goldstein, W. H. 1995, *ApJ*, 438, L115
- Ma, C., Ebeling, H., & Barrett, E. 2009, *ApJ*, 693, L56
- Ma, C., Ebeling, H., Marshall, P., & Schrabback, T. 2010, *MNRAS*, 406, 121
- Mahdavi, A., Hoekstra, H., Babul, A., Balam, D. D., & Capak, P. L. 2007, *ApJ*, 668, 806
- Margoniner, V. E., de Carvalho, R. R., Gal, R. R., & Djorgovski, S. G. 2001, *ApJ*, 548, L143
- Markevitch, M. 2006, in *ESA Special Publication*, Vol. 604, *The X-ray Universe 2005*, ed. A. Wilson, 723–+
- Markevitch, M., Bautz, M. W., Biller, B., Butt, Y., Edgar, R., Gaetz, T., Garmire, G., Grant, C. E., Green, P., Juda, M., Plucinsky, P. P., Schwartz, D., Smith, R., Vikhlinin, A., Virani, S., Wargelin, B. J., & Wolk, S. 2003, *ApJ*, 583, 70
- Markevitch, M., Forman, W. R., Sarazin, C. L., & Vikhlinin, A. 1998, *ApJ*, 503, 77
- Markevitch, M., Gonzalez, A. H., David, L., Vikhlinin, A., Murray, S., Forman, W., Jones, C., & Tucker, W. 2002, *ApJ*, 567, L27
- Markevitch, M., & Vikhlinin, A. 2007, *Phys. Rep.*, 443, 1
- Mastropietro, C., & Burkert, A. 2008, *MNRAS*, 389, 967
- Mathis, H., Lavaux, G., Diego, J. M., & Silk, J. 2005, *MNRAS*, 357, 801
- Maughan, B. J., Ellis, S. C., Jones, L. R., Mason, K. O., Córdova, F. A., & Priedhorsky, W. 2006, *ApJ*, 640, 219
- Maurogordato, S., Cappi, A., Ferrari, C., Benoist, C., Mars, G., Soucail, G., Arnaud, M., Pratt, G. W., Bourdin, H., & Sauvageot, J.-L. 2008, *A&A*, 481, 593
- Merritt, D. 1987, *ApJ*, 313, 121
- Metevier, A. J., Romer, A. K., & Ulmer, M. P. 2000, *AJ*, 119, 1090
- Miller, N. A., Oegerle, W. R., & Hill, J. M. 2006, *AJ*, 131, 2426
- Miller, N. A., & Owen, F. N. 2003, *AJ*, 125, 2427
- Miszalski, B., Shorridge, K., Saunders, W., Parker, Q. A., & Croom, S. M. 2006, *MNRAS*, 371, 1537
- Neumann, D. M., & Böhringer, H. 1997, *MNRAS*, 289, 123
- O'Sullivan, E., Vrtilek, J. M., Kempner, J. C., David, L. P., & Houck, J. C. 2005, *MNRAS*, 357, 1134
- Owers, M. S., Couch, W. J., & Nulsen, P. E. J. 2009a, *ApJ*, 693, 901
- Owers, M. S., Nulsen, P. E. J., Couch, W. J., & Markevitch, M. 2009b, *ApJ*, 704, 1349
- Owers, M. S., Nulsen, P. E. J., Couch, W. J., Markevitch, M., & Poole, G. B. 2009c, *ApJ*, 692, 702
- Pinkney, J., Roettiger, K., Burns, J. O., & Bird, C. M. 1996, *ApJS*, 104, 1
- Poggianti, B. M., Bridges, T. J., Komiyama, Y., Yagi, M., Carter, D., Mobasher, B., Okamura, S., & Kashikawa, N. 2004, *ApJ*, 601, 197
- Poole, G. B., Fardal, M. A., Babul, A., McCarthy, I. G., Quinn, T., & Wadsley, J. 2006, *MNRAS*, 373, 881
- Randall, S., Nulsen, P., Forman, W. R., Jones, C., Machacek, M., Murray, S. S., & Maughan, B. 2008, *ApJ*, 688, 208
- Roettiger, K., Burns, J. O., & Loken, C. 1996, *ApJ*, 473, 651
- Saunders, W., Bridges, T., Gillingham, P., Haynes, R., Smith, G. A., Whittard, J. D., Churilov, V., Lankshear, A., Croom, S., Jones, D., & Boshuizen, C. 2004, in *Presented at the Society of Photo-Optical Instrumentation Engineers (SPIE) Conference*, Vol. 5492, *Ground-based Instrumentation for Astronomy*. Edited by Alan F. M. Moorwood and Iye Masanori. *Proceedings of the SPIE*, Volume 5492, pp. 389-400 (2004)., ed. A. F. M. Moorwood & M. Iye, 389–400
- Sharp, R., Saunders, W., Smith, G., Churilov, V., Correll, D., Dawson, J., Farrel, T., Frost, G., Haynes, R., Heald, R., Lankshear, A., Mayfield, D., Waller, L., & Whittard, D. 2006, in *Presented at the Society of Photo-Optical Instrumentation Engineers (SPIE) Conference*, Vol. 6269, *Ground-based and Airborne Instrumentation for Astronomy*. Edited by McLean, Ian S.; Iye, Masanori. *Proceedings of the SPIE*, Volume 6269, pp. 62690G (2006).
- Smith, G. A., Saunders, W., Bridges, T., Churilov, V., Lankshear, A., Dawson, J., Correll, D., Waller, L., Haynes, R., & Frost, G. 2004, in *Presented at the Society of Photo-Optical Instrumentation Engineers (SPIE) Conference*, Vol. 5492, *Ground-based Instrumentation for Astronomy*. Edited by Alan F. M. Moorwood and Iye Masanori. *Proceedings of the SPIE*, Volume 5492, pp. 410-420 (2004)., ed. A. F. M. Moorwood & M. Iye, 410–420
- Springel, V., & Farrar, G. R. 2007, *MNRAS*, 380, 911
- Springel, V., Frenk, C. S., & White, S. D. M. 2006, *Nature*, 440, 1137
- Tonry, J., & Davis, M. 1979, *AJ*, 84, 1511
- Venturi, T., Bardelli, S., Morganti, R., & Hunstead, R. W. 2000, *MNRAS*, 314, 594
- Venturi, T., Bardelli, S., Zagaria, M., Prandoni, I., & Morganti, R. 2002, *A&A*, 385, 39
- Venturi, T., Bardelli, S., Zambelli, G., Morganti, R., & Hunstead, R. W. 2001, *MNRAS*, 324, 1131
- Vikhlinin, A., Markevitch, M., Murray, S. S., Jones, C., Forman, W., & Van Speybroeck, L. 2005, *ApJ*, 628, 655
- West, M. J., & Bothun, G. D. 1990, *ApJ*, 350, 36
- Wild, V., & Hewett, P. C. 2005, *MNRAS*, 358, 1083
- Zabludoff, A. I., Franx, M., & Geller, M. J. 1993, *ApJ*, 419, 47
- Zabludoff, A. I., & Zaritsky, D. 1995, *ApJ*, 447, L21+
- Zhang, Y., Finoguenov, A., Böhringer, H., Ikebe, Y., Matsushita, K., & Schuecker, P. 2004, *A&A*, 413, 49